NEW RESULTS ON DIFFERENTIAL AND NON–COHERENT TRANSMISSION: MSDD FOR CORRELATED MIMO FADING CHANNELS AND PERFORMANCE ANALYSIS FOR GENERALIZED K–FADING

by

CINDY YUE ZHU

B.ASc., The University of British Columbia, 2007

A THESIS SUBMITTED IN PARTIAL FULFILLMENT OF
THE REQUIREMENTS FOR THE DEGREE OF

MASTER OF APPLIED SCIENCE

in

THE FACULTY OF GRADUATE STUDIES

(Electrical and Computer Engineering)

The University of British Columbia

(Vancouver)

September 2009

Abstract

In this thesis, we revisit differential and non–coherent transmission techniques over fading channels. In particular, we consider receiver design for differential space–time modulation (DSTM) over correlated multiple–input multiple–output (MIMO) fading channels and the performance analysis of differential phase shift keying (DPSK) and non–coherent frequency shift keying (FSK) in generalized K–fading.

For DSTM over spatially correlated MIMO channels, we derive a multiple–symbol differential detection (MSDD) and a novel MSDD–based decision–feedback differential detection (MS–DFDD) receiver. We show that MS–DFDD outperforms previously proposed decision–feedback differential detection (DFDD) schemes that are based on scalar and vector prediction. In addition, we prove that at high signal–to–noise ratio (SNR) vector prediction decision–feedback differential detection (VP–DFDD) is equivalent to scalar prediction decision–feedback differential detection (SP–DFDD) and thus fails to properly exploit the spatial fading correlations.

Furthermore, we derive closed–form expressions for the bit error probability (BEP) of two non–coherent transmission schemes over L diversity branches being subject to generalized K–fading. Specifically, focus is on binary DPSK (DBPSK) and binary non–coherent FSK modulation with equal–gain combining (EGC) at the receiver. We also discuss the extension of our results to M–ary modulation schemes. Considering both independent and correlated fading across the L branches, we derive expressions for the asymptotic diversity order, which reveal an interesting interplay between the two parameters,

k and m, of the generalized K–distribution. Moreover, we show that the diversity order of the considered non–coherent transmission schemes is the same as in the case of coherent transmission. Finally, numerical performance results are presented, and our analytical results are corroborated by means of Monte–Carlo simulation.

Table of Contents

List of Figures

List of Abbreviations and Symbols

Acronyms

AWGN	Additive white Gaussian noise
BEP	Bit error probability
CD	Coherent detection
CDD	Conventional differential detection
CSI	Channel state information
DBPSK	Binary differential phase shift keying
DFDD	Decision–feedback differential detection
DPSK	Differential phase shift keying
DQPSK	Quadrature differential phase shift keying
DSTM	Differential space–time modulation
EGC	Equal–gain combining
FSK	Frequency shift keying
I.I.D	Independent and identically distributed
I.N.D	Independent but not necessarily identically distributed
MGF	Moment generating function
MIMO	Multiple–input multiple–output
MRC	Maximum–ratio combining
MS–DFDD	MSDD–based decision–feedback differential detection
MSDD	Multiple–symbol differential detection
PDF	Probability density function
PEP	Pairwise error probability

PSK	Phase shift keying
QAM	Quadrature amplitude modulation
QPSK	Quadrature phase shift keying
SEP	Symbol error probability
SNR	Signal–to–noise ratio
SP	Scalar predictor
SP–DFDD	Scalar prediction decision–feedback differential detection
VP	Vector predictor
VP–DFDD	Vector prediction decision–feedback differential detection

Operators and Notation

$\lvert\cdot\rvert$	Absolute value of a complex number
$\mathcal{E}\{\cdot\}$	Expectation
$[\cdot]^*$	Complex conjugate
$[\cdot]^T$	Matrix or vector transposition
$[\cdot]^H$	Matrix or vector Hermitian transposition
$\boldsymbol{I}_m$	Identity matrix with dimension $m \times m$
$\doteq$	Asymptotic equality
$\otimes$	Kronecker product
$\mathrm{diag}\{\boldsymbol{x}\}$	Diagonal matrix with the elements of vector $\boldsymbol{x}$ in its main diagonal
$[\mathbf{X}]_{i,j}$	Element in row i and column j of matrix $\mathbf{X}$

Acknowledgments

I would like to express my sincere appreciation toward my supervisor, Dr. Robert Schober, for his outstanding supervision, support and encouragement throughout my research projects. Professor Schober provided much of the initial motivation for pursuing this investigation and also provided priceless feedback that has improved this work in nearly every aspect. In addition, I would like to thank Dr. Simon Yiu and Dr. Jan Mietzner for their help in my research.

Finally, I would like to thank my family for their support and encouragement in my quest for higher education. I would also like to extend my thanks to the colleagues at the Department of Electrical and Computer Engineering, UBC, for creating a stimulating and a friendly environment at work.

Cindy Yue Zhu

The University of British Columbia
Vancouver, Canada
July 2009

Chapter 1

1 Introduction

The following section provides an overview of the background information and motivation for this work in detail. We also review the related work that has been reported by other researchers in this field. The contributions of this work are briefly summarized in the second section of this chapter, and the concluding section outlines the organization of this thesis.

1.1 Background and Motivation

In recent years, the application of multiple antennas in different wireless communication environments has received considerable interest from academia and industry. In particular, in practical cases where accurate channel knowledge at the receiver is not available, differential and non–coherent transmission schemes eliminate the need for channel estimation at the receiver and are thus attractive for high–mobility and low SNR scenarios as well as for low–cost receiver implementations. DPSK and DSTM [1] are popular modulation schemes if channel state information (CSI) is not available at the receiver side. Since conventional differential detection (CDD) causes significant performance degradations compared to coherent detection (CD) in time–variant fading channels, in the last few years various DFDD and MSDD schemes have been proposed for performance improvement, cf. e.g. [2, 3]. However, while

in practice the fading gains may be spatially correlated due to insufficient antenna spacing, [2, 3] only considered the spatially uncorrelated case. The performance of DSTM and beamforming for DSTM in spatially correlated fading were considered in [4] and [5, 6], respectively. However, the detection scheme applied in [4, 5, 6] was simple CDD which does not take into account spatial correlations. A sequence–detection based non–coherent detection scheme taking into account spatial fading correlations was proposed in [7]. Interestingly, if the number of trellis states of the sequence–detection based scheme in [7] is reduced to zero, it can be interpreted as DFDD for correlated fading, where the DFDD coefficients are the coefficients of a scalar predictor (SP) or a vector predictor (VP) for the fading–plus–noise process. Thus, we refer to the corresponding detectors as SP–DFDD and VP–DFDD, respectively.

Since the transmission environment is essential to a wireless communication system, we also investigate the generalized K–fading model. The performance of wireless communication systems is largely governed by shadowing and multipath fading effects [8, Ch. 2]. While major obstacles between transmitter and receiver cause macroscopic fading effects, i.e., fluctuations in the average received SNR, scatterers in the vicinity of transmitter and receiver entail microscopic fading effects, i.e., fluctuations in the instantaneous received SNR. The generalized K–fading model is characterized by two parameters, $k > 0$ and $m > 0$, which accurately capture the effects of composite shadowing and multipath fading. In particular, it comprises a large variety of channel conditions, ranging from severe shadowing (small values of k) to mild shadowing (large values of k) and from severe multipath fading (small values of m) to mild multipath fading (large values of m). Moreover, the generalized K–fading model can also be employed to model cascade multipath fading, which occurs, e.g., in keyhole and in mobile–to–mobile communication scenarios [9], [10]. For the special case where $k = m = 1$, the generalized K–fading model reduces to the double Rayleigh–fading model. By varying the fading parameters accordingly, more or less severe cascade multipath fading can be modeled.

A favorable property of the generalized K–fading model is that it allows for a closed–form expression for the probability density function (PDF) of the instantaneous received SNR, which is in contrast to, e.g., competing composite shadowing/multipath fading models that are based on the lognormal PDF. As a result, several analytical performance results for generalized K–fading and ordinary K–fading (when $m = 1$) have been reported in the literature. Moreover, analytical performance results for the special case of double Rayleigh fading were presented in [10, 11, 12].

Most of the papers mentioned above have focused on coherent transmission schemes, which rely on the availability of accurate channel knowledge at the receiver side. However, since non–coherent transmission schemes eliminate the need for channel estimation at the receiver, we derive closed–form expressions for the BEP of two non–coherent transmission schemes over L generalized K–fading branches with (post–detection) EGC at the receiver. Specifically, focus is on DBPSK modulation with CDD at the receiver (i.e., based on two subsequent received symbols) and orthogonal binary frequency–shift keying (FSK) modulation with non–coherent detection at the receiver [13, Ch. 9.4]. We also discuss the extension of our results to M–ary modulation schemes. Concerning the K–fading model we consider two scenarios. First, we focus on the case of independent fading across the L branches. This scenario appears to be relevant for cascade multipath fading, if the underlying assumption is a rich–scattering radio environment (see [10] for examples). Here, the assumption of uncorrelated diversity branches – created, e.g., by multiple receive antennas with sufficiently large antenna spacing – appears to be reasonable. Afterwards, we turn to the case of composite shadowing and multipath fading. Here, we consider the scenario where the shadowing part is fully correlated across links, whereas the multipath fading is independent and identically distributed (i.i.d.) across the L branches. Since shadowing represents a large–scale fading effect, it can be expected to affect all diversity branches simultaneously, while in a rich–scattering environment the multipath fading part can again be considered

independent across links. For both scenarios, we present a high–SNR analysis and provide expressions for the resulting asymptotic diversity orders, which reveal an interesting interplay between the two fading parameters k and m. It is worth noting that the existing papers on non–coherent transmission schemes over generalized K–fading or double Rayleigh–fading links [10]-[14, 15] are all restricted to a single branch ($L = 1$). In particular, to the best of our knowledge closed–form expressions for the BEP and the asymptotic diversity order of the considered non–coherent transmission schemes in generalized K–fading have not yet been presented in the literature.

1.2 Contributions

The main contributions of the present research work are as follows:

- We derive an MSDD and a low-complexity MS–DFDD receiver for DSTM transmitted over spatially correlated MIMO fading channels. The proposed DFDD scheme is obtained by introducing decision-feedback symbols into the MSDD metric. We show that MS-DFDD outperforms both SP–DFDD and VP–DFDD. Furthermore, we prove that at high SNR SP–DFDD and VP–DFDD are equivalent. Thus, at high SNR VP-DFDD does not result in performance gains compared to the simpler SP-DFDD.

- We also derive closed–form expressions for the BEP of two non–coherent transmission schemes over L generalized K–fading branches with EGC at the receiver. Specifically, focus is on DBPSK and binary non–coherent FSK modulation. Note that the existing papers on non-coherent transmission schemes over (generalized) K–fading or double Rayleigh–fading links are all restricted to the case of a single link ($L = 1$).

  - First, we focus on the case of i.i.d. fading across the L branches, which appears to be relevant for the case of cascade multipath fad-

ing.

  - We then turn to the case of composite shadowing and multipath fading. Here, we consider the scenario where the shadowing part is fully correlated across links, whereas the multipath fading is i.i.d. across the L branches. For both cases, we present a high–SNR analysis and state expressions for the resulting asymptotic diversity order, which reveal an interesting interplay between the two fading parameters k and m.

The results of our work are summarized in the following papers:

- C. Zhu, S. Yiu, and R. Schober. On Noncoherent Receivers for DSTM in Spatially Correlated Fading. *Accepted for publication in the IEEE Transactions on Communications*, December 2008.

- C. Zhu, J. Mietzner, and R. Schober. On the Performance of Non–Coherent Transmission Schemes over Multiple Generalized K–Fading Links. *Submitted to the IEEE Transaction of Wireless Communications*, February 2009.

- C. Zhu, J. Mietzner, and R. Schober. On the Performance of Non–Coherent Transmission Schemes with Equal–Gain Combining in Correlated Generalized K–Fading. *Accepted for presentation at the IEEE Vehicular Technology Conference*, Anchorage, Alaska, USA, September 2009.

1.3 Thesis Organization

To explain the above findings in detail, this thesis is organized as follows. In Chapter 2, we will describe DSTM in detail. The proposed differential detectors for DPSK and DSTM are also discussed in this chapter. The simulations results for the improved differential detectors are also provided. In Chapter

3, the generalized K–fading model is introduced. The performance analysis of both binary and M–ary modulation over generalized K–fading channels is discussed in Chapters 4 and 5, respectively. The simulation results for the generalized K–fading channels are provided also included in Chapter 5, and some conclusions are given in Chapter 6.

Chapter 2

1 Non–Coherent Detectors for DPSK and DSTM

In this section, we first give a brief introduction to DSTM followed by the derivation of the optimum MSDD decision rule and the related MS–DFDD scheme for spatially correlated fading channels. We also compare MS–DFDD with SP–DFDD and VP–DFDD.

2.1 System Model

In this section, we assume a MIMO channel with N_T transmit and N_R receive antennas. In DSTM, the data–carrying $N_T \times N_T$ matrix symbols $\boldsymbol{V}[k]$ are taken from a suitable alphabet $\mathcal{V}$ of unitary matrices [1]. Here, k denotes the matrix symbol index and the $N_T \times N_T$ transmit symbol $\boldsymbol{S}[k]$ is obtained from $\boldsymbol{V}[k]$ via differential encoding $\boldsymbol{S}[k] = \boldsymbol{V}[k]\boldsymbol{S}[k-1]$. For the special case when $N_T = 1$, DSTM simplifies to DPSK.

The signals received at the N_R receive antennas in N_T consecutive symbol intervals are collected in a column vector

$$\boldsymbol{r}[k] = \boldsymbol{B}[k]\boldsymbol{h}[k] + \boldsymbol{n}[k], \tag{2.1}$$

where $\boldsymbol{r}[k] \triangleq [r_{11}[k] \ldots r_{N_T1}[k]\ r_{12}[k] \ldots r_{N_TN_R}[k]]^T$, $\boldsymbol{h}[k] \triangleq [h_{11}[k] \ldots h_{N_T1}[k]\ h_{12}[k] \ldots h_{N_TN_R}[k]]^T$, $\boldsymbol{n}[k] \triangleq [n_{11}[k] \ldots n_{N_T1}[k]\ n_{12}[k] \ldots n_{N_TN_R}[k]]^T$, and

$\boldsymbol{B}[k] \triangleq \boldsymbol{I}_{N_R} \otimes \boldsymbol{S}[k]$. $r_{n_t n_r}[k]$, $h_{n_t n_r}[k]$, and $n_{n_t n_r}[k]$ denote the received signal, the fading gain, and the noise, respectively, corresponding to transmit antenna n_t, $1 \leq n_t \leq N_T$, and receive antenna n_r, $1 \leq n_r \leq N_R$. The Rayleigh fading component $\boldsymbol{h}[k]$ is modeled as a zero–mean Gaussian random vector with correlation matrix $\mathcal{E}\{\boldsymbol{h}[k]\boldsymbol{h}^H[k]\} = \boldsymbol{R}_{\text{rx}} \otimes \boldsymbol{R}_{\text{tx}}$, where $\boldsymbol{R}_{\text{rx}}$ and $\boldsymbol{R}_{\text{tx}}$ denote the $N_R \times N_R$ receive and the $N_T \times N_T$ transmit correlation matrices respectively and $\mathcal{E}\{\cdot\}$ denotes statistical expectation. The temporal fading correlation is modeled as $R_{\text{t}}[\lambda] \triangleq \mathcal{E}\{h_{n_t n_r}[k+\lambda]h^*_{n_t n_r}[k]\} = J_0(2\pi B_f T N_T \lambda)$ [16], where $J_0(\cdot)$, B_f, and T denote the zeroth order Bessel function of the first kind, the Doppler bandwidth, and the symbol interval, respectively. $n_{n_t n_r}[k]$ is spatially and temporally i.i.d. additive white Gaussian noise (AWGN) with variance $\sigma_n^2 \triangleq \mathcal{E}\{|n_{n_t n_r}[k]|^2\}$.

2.2 Noncoherent Detectors

2.2.1 MSDD

To derive the MSDD decision rule we first collect N received vectors $\boldsymbol{r}[k]$ in a new vector $\boldsymbol{r} \triangleq [\boldsymbol{r}^T[k]\ \boldsymbol{r}^T[k-1]\ \ldots\ \boldsymbol{r}^T[k-N+1]]^T$ which can be modeled as

$$\boldsymbol{r} = \boldsymbol{B}\boldsymbol{h} + \boldsymbol{n}, \tag{2.2}$$

with $\boldsymbol{B} \triangleq \text{diag}\{\boldsymbol{B}[k]\ \ldots\ \boldsymbol{B}[k-N+1]\}$, $\boldsymbol{h} \triangleq [\boldsymbol{h}^T[k]\ \ldots\ \boldsymbol{h}^T[k-N+1]]^T$, and $\boldsymbol{n} \triangleq [\boldsymbol{n}^T[k]\ \ldots\ \boldsymbol{n}^T[k-N+1]]^T$. From (2.2) we observe that the PDF $p(\boldsymbol{r}|\boldsymbol{B})$ of $\boldsymbol{r}$ conditioned on $\boldsymbol{B}$ is a zero–mean Gaussian PDF with covariance matrix $\boldsymbol{B}\boldsymbol{R}\boldsymbol{B}^H$, where $\boldsymbol{R} \triangleq \mathcal{E}\{\boldsymbol{h}\boldsymbol{h}^H\} + \mathcal{E}\{\boldsymbol{n}\boldsymbol{n}^H\} = \boldsymbol{R}_{\text{t}} \otimes \boldsymbol{R}_{\text{rx}} \otimes \boldsymbol{R}_{\text{tx}} + \sigma_n^2 \boldsymbol{I}_{NN_RN_T}$ with $[\boldsymbol{R}_{\text{t}}]_{i,j} = R_{\text{t}}[i-j]$, $0 \leq i, j \leq N-1$. Thus, performing maximum–likelihood detection leads to the MSDD decision rule

$$\begin{aligned}\hat{\boldsymbol{V}} &= \underset{\boldsymbol{V}\in\mathcal{V}^{N-1},\ [k-N+1]\in\mathcal{S}}{\operatorname{argmax}} \{p\left(\boldsymbol{r}|\boldsymbol{B}\right)\} \\ &= \underset{\boldsymbol{V}\in\mathcal{V}^{N-1},\ [k-N+1]\in\mathcal{S}}{\operatorname{argmin}} \{\boldsymbol{r}^H\boldsymbol{B}\boldsymbol{R}^{-1}\boldsymbol{B}^H\boldsymbol{r}\},\end{aligned} \tag{2.3}$$

where $\boldsymbol{V} \triangleq [\boldsymbol{V}[k] \ldots \boldsymbol{V}[k-N+2]]$, $\hat{\boldsymbol{V}}$ is the estimate of $\boldsymbol{V}$, and $\mathcal{S}$ is the alphabet of the transmit symbols $\boldsymbol{S}[k]$. We note that for DSTM constellations that form a group $\mathcal{S} = \mathcal{V}$ holds [1]. For further development of (2.3) , the Cholesky factorization of $\boldsymbol{R}^{-1} = \boldsymbol{U}^H\boldsymbol{U}$ is introduced. We partition the upper triangular matrix $\boldsymbol{U}$ into $N_TN_R \times N_TN_R$ sub–matrices $\boldsymbol{U}_{i,j}$, $0 \le i,j \le N-1$ [17]. Thus, (2.3) can be rewritten as

$$\hat{\boldsymbol{V}} = \underset{\boldsymbol{V}\in\mathcal{V}^{N-1},[k-N+1]\in\mathcal{S}}{\operatorname{argmin}} \left\{ \sum_{i=0}^{N-1} \left\| \sum_{j=i}^{N-1} \boldsymbol{U}_{i,j}\boldsymbol{B}^H[k-j]\boldsymbol{r}[k-j] \right\|^2 \right\}. \tag{2.4}$$

For spatially uncorrelated fading we can show that $\boldsymbol{U}_{i,j} \triangleq u_{i,j}^{\mathrm{t}}\boldsymbol{I}_{N_TN_R}$ with $u_{i,j}^{\mathrm{t}} \triangleq [\boldsymbol{U}_{\mathrm{t}}]_{i,j}$ where $\boldsymbol{U}_{\mathrm{t}}$ denotes an upper triangular matrix obtained by Cholesky factorization of $\boldsymbol{R}_{\mathrm{t}} + \sigma_n^2\boldsymbol{I}_N$. Therefore, in this special case, (2.4) is the well–known MSDD decision rule for uncorrelated fading, cf. e.g. [16, 18]. Since the complexity of MSDD grows exponentially with the observation window size N, in the next section, we will introduce MS–DFDD whose complexity grows only linearly with N.

2.2.2 MS–DFDD

The fundamental idea of MS–DFDD is to replace $\boldsymbol{V}[k-j]$, $1 \le j \le N-2$, and $\boldsymbol{S}[k-N+1]$ in (2.4) by the corresponding previously decided symbols $\hat{\boldsymbol{V}}[k-j]$ and $\hat{\boldsymbol{S}}[k-N+1]$. After all irrelevant terms are neglected, this leads to the MS–DFDD decision rule given by

$$\hat{\boldsymbol{V}}[k] = \underset{\boldsymbol{V}[k]\in\mathcal{V}}{\operatorname{argmin}} \left\{ \left\| \boldsymbol{E}\left(\tilde{\boldsymbol{B}}^H[k]\boldsymbol{r}[k] + \sum_{j=1}^{N-1} \boldsymbol{P}_j\hat{\boldsymbol{B}}^H[k-j]\boldsymbol{r}[k-j] \right) \right\|^2 \right\}, \tag{2.5}$$

where $\boldsymbol{E} \triangleq \boldsymbol{U}_{0,0}$, $\boldsymbol{P}_j \triangleq \boldsymbol{U}_{0,0}^{-1}\boldsymbol{U}_{0,j}$, $1 \leq j \leq N-1$, $\hat{\boldsymbol{B}}[k] \triangleq \boldsymbol{I}_{N_R} \otimes \hat{\boldsymbol{S}}[k]$, $\hat{\boldsymbol{S}}[k] = \hat{\boldsymbol{V}}[k]\hat{\boldsymbol{S}}[k-1]$, and $\tilde{\boldsymbol{B}}[k] \triangleq \boldsymbol{I}_{N_R} \otimes (\boldsymbol{V}[k]\hat{\boldsymbol{S}}[k-1])$. Since the $\boldsymbol{U}_{i,j}$ are obtained through Cholesky factorization of $\boldsymbol{R}^{-1}$, it can be shown that the $\boldsymbol{P}_j$ are the coefficients of the optimum linear $(N-1)$th order VP for the fading–plus–noise process $\boldsymbol{f}[k] \triangleq \boldsymbol{h}[k] + \boldsymbol{n}[k]$ [17], i.e., the $\boldsymbol{P}_j$ minimize the prediction error variance $\sigma_e^2 \triangleq \mathcal{E}\{||\boldsymbol{e}[k]||^2\}$ with

$$\boldsymbol{e}[k] \triangleq \boldsymbol{f}[k] - \sum_{j=1}^{N-1} \boldsymbol{P}_j \boldsymbol{f}[k-j]. \tag{2.6}$$

Furthermore, $(\boldsymbol{E}^H\boldsymbol{E})^{-1} = (\boldsymbol{U}_{0,0}^H\boldsymbol{U}_{0,0})^{-1}$ can be shown to be the covariance matrix of the prediction error, i.e., $\boldsymbol{R}_{ee} \triangleq \mathcal{E}\{\boldsymbol{e}[k]\boldsymbol{e}^H[k]\} = (\boldsymbol{U}_{0,0}^H\boldsymbol{U}_{0,0})^{-1}$. Consequently, (2.5) can be interpreted as temporal linear vector prediction with subsequent spatial prediction error whitening. We note that for the special case of spatially uncorrelated fading $\boldsymbol{E} = u_{0,0}^{\mathrm{t}}\boldsymbol{I}_{N_TN_R}$ and $\boldsymbol{P}_j = (u_{0,j}^{\mathrm{t}}/u_{0,0}^{\mathrm{t}})\boldsymbol{I}_{N_TN_R}$, where $(u_{0,0}^{\mathrm{t}})^{-2}$ and $u_{0,j}^{\mathrm{t}}/u_{0,0}^{\mathrm{t}}$, $1 \leq j \leq N-1$, denote the error variance and the coefficients of the optimum $(N-1)$th order SP for the scalar fading–plus–noise process $f_{n_tn_r}[k] \triangleq h_{n_tn_r}[k] + n_{n_tn_r}[k]$. Thus, in this case, (2.5) is equivalent to the DFDD scheme proposed in [16] for spatially independent fading.

2.2.3 The Relationship between MS–DFDD and SP–/VP–DFDD

It is of interest to compare the MS–DFDD decision rule in (2.5) with SP–DFDD and VP–DFDD, which can be obtained as special cases of the sequence detection scheme in [7] if the number of trellis states is reduced to zero. In particular, by letting $\boldsymbol{E} = \boldsymbol{I}_{N_TN_R}$ and $\boldsymbol{P}_j = (u_{0,j}^{\mathrm{t}}/u_{0,0}^{\mathrm{t}})\boldsymbol{I}_{N_TN_R}$, $1 \leq j \leq N-1$, (2.5) simplifies to the SP–DFDD metric in [7, Eq. (5)]. Obviously, SP–DFDD completely ignores the fading correlations. The VP–DFDD metric in [7, Eq. (10)] is obtained by letting $\boldsymbol{E} = \boldsymbol{I}_{N_TN_R}$ and $\boldsymbol{P}_j \triangleq \boldsymbol{U}_{0,0}^{-1}\boldsymbol{U}_{0,j}$, $1 \leq j \leq N-1$, in (2.5). Thus, similar to MS–DFDD, VP–DFDD contains an optimum linear VP. However, in contrast to MS–DFDD, spatial whitening of the prediction

error is not performed in VP–DFDD. We will show in Section 2.4 that this might have some unexpected consequences. It is also worth noting that, similar to the schemes in [7, 19], the metric in (2.5) can also be used as branch metric in a Viterbi algorithm. This leads to an improved performance as compared to DFDD since error propagation is mitigated but increases receiver complexity.

For this purpose, we compare all three DFDD schemes for the case $\sigma_n^2 \to 0$. Define $\tilde{\boldsymbol{R}}_{\mathrm{t}}$ as the $(N-1)\times(N-1)$ lower sub–block matrix of $N\times N$ matrix $\boldsymbol{R}_{\mathrm{t}}$, $\boldsymbol{r}_{\mathrm{t}} \triangleq [R_{\mathrm{t}}[-1] \ \ldots \ R_{\mathrm{t}}[-(N-1)]]^T$, and $\boldsymbol{P} \triangleq [\boldsymbol{P}_1^T \ \ldots \ \boldsymbol{P}_{N-1}^T]^T$. The Yule–Walker equation for the optimum VP is given by

$$(\tilde{\boldsymbol{R}}_{\mathrm{t}} \otimes \boldsymbol{R}_{\mathrm{rx}} \otimes \boldsymbol{R}_{\mathrm{tx}} + \sigma_n^2 \boldsymbol{I}_{(N-1)N_T N_R})\boldsymbol{P} = \boldsymbol{r}_{\mathrm{t}} \otimes \boldsymbol{R}_{\mathrm{rx}} \otimes \boldsymbol{R}_{\mathrm{tx}}. \tag{2.7}$$

We observe from (2.7) that for $\sigma_n^2 \to 0$ the optimum VP coefficients are given by $\boldsymbol{P} = (\tilde{\boldsymbol{R}}_{\mathrm{t}}^{-1}\boldsymbol{r}_{\mathrm{t}}) \otimes \boldsymbol{I}_{N_T N_R}$. Since vector $\tilde{\boldsymbol{R}}_{\mathrm{t}}^{-1}\boldsymbol{r}_{\mathrm{t}}$ contains the coefficients of the optimum scalar predictor of length $N-1$, we conclude that surprisingly for $\sigma_n^2 \to 0$ VP–DFDD simplifies to SP–DFDD. Similarly, it can be shown that for $\sigma_n^2 \to 0$ the prediction error covariance matrix becomes $\boldsymbol{R}_{ee} = (1 - \boldsymbol{r}_{\mathrm{t}}^H \tilde{\boldsymbol{R}}_{\mathrm{t}}^{-1}\boldsymbol{r}_{\mathrm{t}})(\boldsymbol{R}_{\mathrm{rx}} \otimes \boldsymbol{R}_{\mathrm{tx}})$, i.e., $\boldsymbol{E} = (\boldsymbol{R}_{\mathrm{rx}} \otimes \boldsymbol{R}_{\mathrm{tx}})^{-1/2}/\sqrt{1 - \boldsymbol{r}_{\mathrm{t}}^H \tilde{\boldsymbol{R}}_{\mathrm{t}}^{-1}\boldsymbol{r}_{\mathrm{t}}}$. Therefore, unlike VP–DFDD, MS–DFDD exploits spatial fading correlations also for high SNR.

As mentioned before, the complexity of all considered DFDD schemes is linear in N. However, for metric calculation SP–DFDD requires the smallest number of multiplications, whereas MS–DFDD requires the most. In particular, for SP–DFDD all predictor coefficients are scalars and $\boldsymbol{E}$ can be omitted in (2.5), while for MS–DFDD, in general, all predictor coefficients are $N_T N_R \times N_T N_R$ matrices and $\boldsymbol{E}$ cannot be omitted. The complexity of VP–DFDD is between that of SP–DFDD and MS–DFDD since the predictor coefficients are matrices but $\boldsymbol{E}$ can be omitted in (2.5).

2.3 Performance Analysis

The performance analysis of MSDD and DFDD in correlated fading closely follows the corresponding analyses for the uncorrelated case in [16, 18]. Therefore, we only give a brief sketch of the analysis here. To simplify our exposition, we assume group codes in which case the elements $\boldsymbol{V}_l$, $0 \leq l \leq L-1$, of $\mathcal{V}$ are diagonal matrices [1].

The BEP of DFDD can be approximated as $P_b \approx \frac{x_e}{RN_T} \sum_{l=1}^{L-1} P_e(\boldsymbol{V}_l \rightarrow \boldsymbol{V}_0)$ [16, Eqs. (45)–(47)], where R and $P_e(\boldsymbol{V}_l \rightarrow \boldsymbol{V}_0)$ are the rate of the considered DSTM scheme and the pairwise error probability (PEP) assuming $\hat{\boldsymbol{S}}[k-j] = \boldsymbol{S}[k-j]$, $1 \leq j \leq N-1$ (genie–aided DFDD), respectively. If decision feedback is not required, $x_e = 1$, otherwise $x_e = 2$. Based on (2.5) it can be shown that since the $\boldsymbol{V}_l$, $0 \leq l \leq L-1$, are diagonal matrices, feedback is not needed for $N = 2$ for SP–DFDD. In contrast, for VP–DFDD and MS–DFDD feedback in form of $\hat{\boldsymbol{S}}[k-1]$ is required even for $N = 2$ except for the special case of DPSK ($N_T = 1$). The PEP $P_e(\boldsymbol{V}_l \rightarrow \boldsymbol{V}_0)$ itself can be obtained using standard tools, cf. e.g. [16, 18] and references therein, since the corresponding metric difference is a quadratic form of Gaussian random variables.

Similarly, for MSDD the metric difference is also a Gaussian quadratic form and the approach outlined in [18, Section IV] can be used to compute an approximation for the BEP based on the PEPs.

2.4 Simulation and Numerical Results

In this section, we compare optimum MSDD, MS–DFDD, SP–DFDD, and VP–DFDD based on simulations and numerical results. For all results a normalized Doppler bandwidth of $B_f T = 0.05$ is assumed.

In Fig. 2.1, we show the BEP of the considered detection strategies for diagonal DSTM [1] vs. E_b/N_0 (E_b: received energy per bit, N_0: single–sided power spectral density of the underlying continuous–time noise process). $N_T = 2$,

$N_R = 1$, $R = 2$ bit/(channel use), and the correlation between both transmit antennas is $\rho = 0.9$.[1] For $N = 2$ we observe from Fig. 2.1 that while MSDD leads to substantial performance gains compared to SP- and VP–DFDD, this is not true for the proposed MS–DFDD. For $N = 2$ MS–DFDD is negatively affected by error propagation negating any potential performance gains over SP- and VP–DFDD which both do not suffer from error propagation in this case. In contrast, for $N = 3$ all DFDD schemes are affected by error propagation and MS–DFDD yields substantial gains compared to SP- and VP–DFDD, especially in the error floor region. For low–to–medium SNRs (e.g. $E_b/N_0 = 15$ dB) all considered DFDD schemes have a comparable performance, while MSDD still yields considerable gains. For $N = 10$, where simulation of MSDD is too time consuming because of its high complexity, MS–DFDD achieves a gain of approximately 0.6 dB at BEP $= 10^{-6}$ compared to VP–DFDD. However, even for $N = 10$ the performance gap between MS–DFDD and CD is quite large because of the relatively large normalized Doppler bandwidth. For $N = 2$ and $N = 3$ SP–DFDD and VP–DFDD achieve a similar performance in the considered range of SNRs. In contrast, for $N = 10$ VP–DFDD outperforms SP–DFDD, especially for $E_b/N_0 \geq 20$ dB. We note that the theoretical results (solid lines) obtained with the methods outlined in Section 2 agree well with the simulation results (markers) at high SNR.

In Fig. 2.2, we consider the same detection schemes as in Fig. 2.1. However, now quaternary DPSK (DQPSK) transmission with $N_T = 1$ and $N_R = 2$ is assumed, and the two receive antennas have correlation $\rho = 0.9$. We observe that both MS–DFDD and MSDD yield substantial performance gains compared to SP- and VP–DFDD, especially in the error floor region. Since unlike for DSTM with $N_T \geq 2$, for single–antenna transmission feedback is not required for MS–DFDD with $N = 2$, MS–DFDD also outperforms SP- and VP–DFDD in this case.

[1] We note that experiments have shown that antenna correlations of $\rho = 0.9$ and more can occur for example in small handsets accommodating multiple antennas [20].

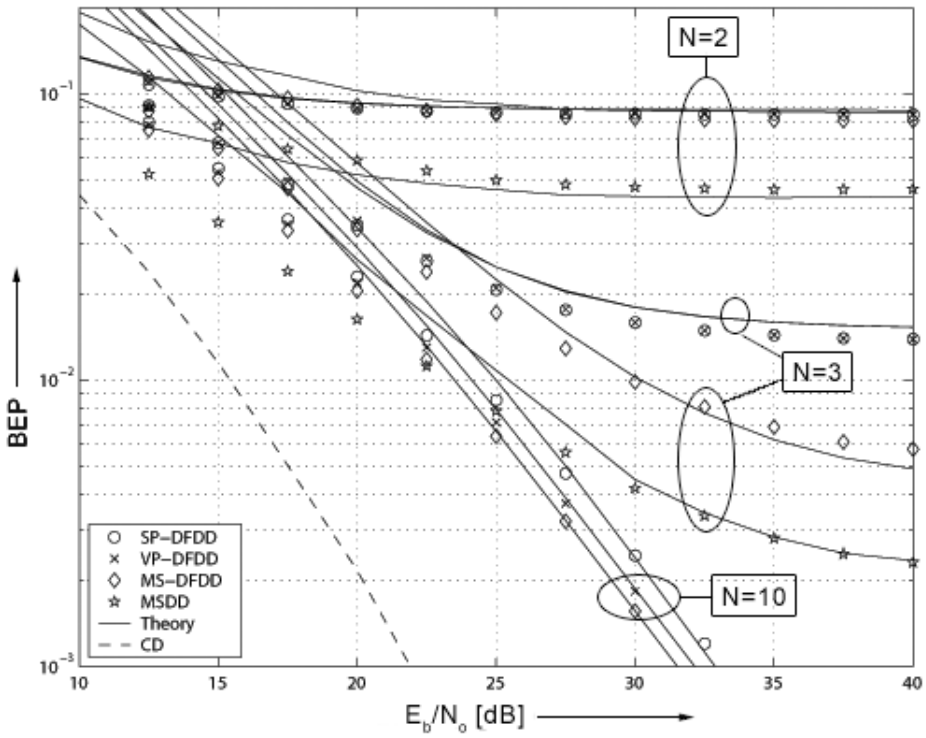

Figure 2.1: BEP of SP–DFDD, VP–DFDD, MS–DFDD (proposed), and MSDD (proposed) vs. E_b/N_0 for diagonal DSTM with $R = 2$ bit/(channel use), $N_T = 2$, $N_R = 1$, $\rho = 0.9$, and $B_f T = 0.05$. Numerical results: Solid lines. Simulation results: Markers.

In Figs. 2.3 and 2.4, we show the simulated error floor ($E_b/N_0 \to \infty$) of diagonal DSTM ($N_T = 2$, $N_R = 1$, $R = 2$ bit/(channel use)) and DQPSK ($N_T = 1$, $N_R = 2$) caused by the various considered receivers as a function of the transmit/receive antenna correlation ρ, respectively. As expected, for $\rho = 0$ SP-, VP-, and MS–DFDD yield the same performance as these schemes are identical in this case. However, as ρ increases, both MS–DFDD and MSDD outperform SP–DFDD and VP–DFDD, which yield identical performance, cf. Section 2.2.3. Interestingly, Fig. 2.3 shows that the performance of MS–DFDD and MSDD may even improve with increasing ρ, whereas that of SP–DFDD and VP–DFDD always deteriorates. In order to explain this observation, two different effects have to be taken into account. On the one hand, the spatial diversity, and thus the performance, is negatively affected

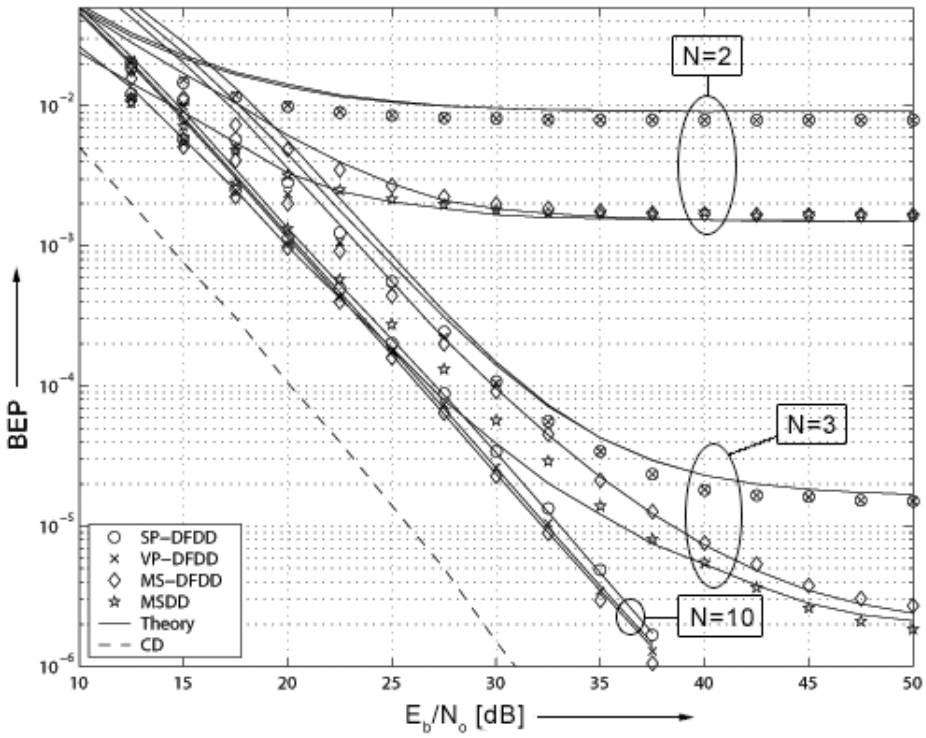

Figure 2.2: BEP of SP–DFDD, VP–DFDD, MS–DFDD (proposed), and MSDD (proposed) vs. E_b/N_0 for DQPSK, $N_T = 1$, $N_R = 2$, $\rho = 0.9$, and $B_f T = 0.05$. Numerical results: Solid lines. Simulation results: Markers.

by increasing ρ. On the other hand, spatial fading correlations lead to spatial correlations in the prediction error vector $\boldsymbol{e}[k]$, which constitutes the effective noise vector for detection purpose, cf. Section 2.2.3, (2.5), (2.6). These correlations in the prediction error are beneficial if they are properly exploited by the detector. Since both MS–DFDD and MSDD exploit the spatial correlation in the prediction error vector, their performance improves with increasing ρ if this positive effect of spatial correlation outweighs the negative effect of the decreased diversity. In contrast, the performance of SP–DFDD and VP–DFDD always deteriorates with increasing spatial fading correlation since these schemes do not exploit the resulting spatial correlation of the prediction error vector.

In Figs. 2.1 to 2.4, we have assumed that the spatial and temporal correlations as well as the operating SNR are perfectly known for DFDD and MSDD

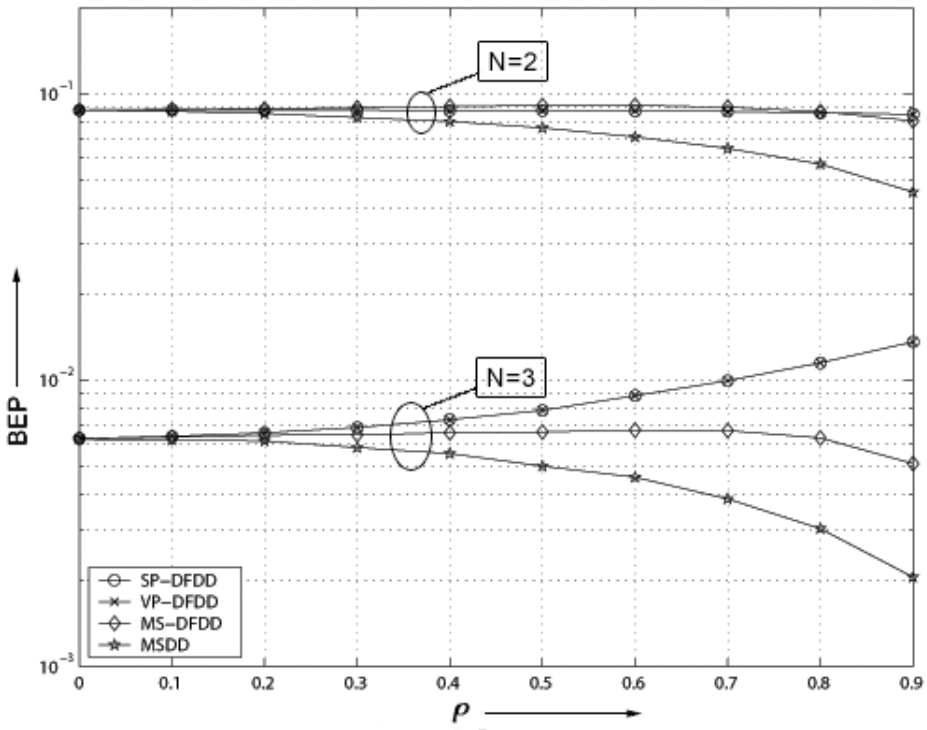

Figure 2.3: BEP of SP–DFDD, VP–DFDD, MS–DFDD (proposed), and MSDD (proposed) vs. transmit antenna correlation ρ for diagonal DSTM with $R = 2$ bit/(channel use), $N_T = 2$, $N_R = 1$, $E_b/N_0 \to \infty$, and $B_f T = 0.05$. Simulation results.

design. In a practical scenario, these parameters are not known *a priori* and have to be estimated by the receiver which may lead to a mismatch between the estimated channel parameters and the true channel parameters. The effects of such a mismatch are investigated in Fig. 2.5 for diagonal DSTM ($N_T = 2$, $N_R = 1$, $R = 2$ bit/(channel use)). In Fig. 2.5, we show the BEP as a function of $B_f T$ for different ρ and E_b/N_0 adopting mismatched estimated channel parameters of $\widehat{B_f T} = 0.05$, $\hat{\rho} = 0.6$, and $\widehat{E_b/N_0} = 35$ dB for receiver design. In Fig. 2.5a), the performance of VP–DFDD (solid lines) and MS–DFDD (dashed lines) are compared under these conditions for $N = 3$. As can be observed, even for mismatched channel parameters MS–DFDD outperforms VP–DFDD in all cases for the considered parameter range. In Fig. 2.5b), the performances of MS–DFDD with mismatched (solid lines) and matched (dashed lines) chan-

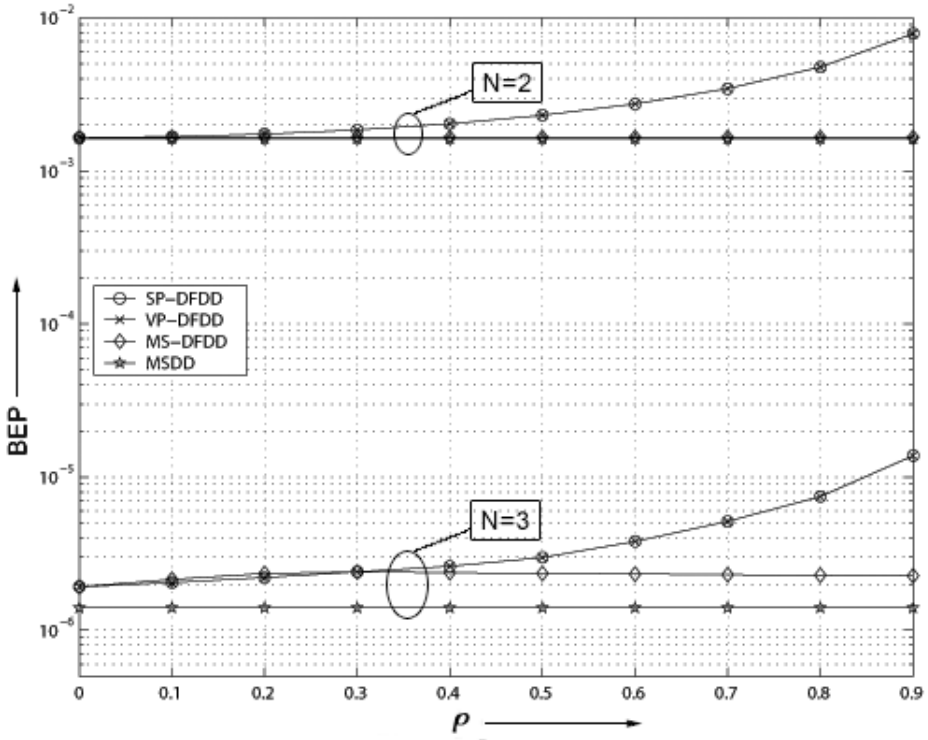

Figure 2.4: BEP of SP–DFDD, VP–DFDD, MS–DFDD (proposed), and MSDD (proposed) vs. receive antenna correlation ρ for DQPSK, $N_T = 1$, $N_R = 2$, $E_b/N_0 \to \infty$, and $B_f T = 0.05$. Simulation results.

nel parameters are compared for $N = 5$. In the mismatched case, the estimated channel parameters ($\widehat{B_f T} = 0.05$, $\hat{\rho} = 0.6$, and $\widehat{E_b/N_0} = 35$ dB) were used for MS–DFDD design, whereas in the matched case the true channel parameters were employed. As expected, Fig. 2.5b) shows that mismatch causes a certain performance degradation.

We note that in practice the predictor coefficients $\boldsymbol{P}_j$, $1 \leq j \leq N-1$, and the prediction error covariance matrix $\boldsymbol{R}_{ee}$ may be directly computed using an adaptive algorithm, which would avoid the need for explicit estimation of the channel parameters. For this purpose, the approach presented in [21] for scalar DFDD may be extended to the vector case.

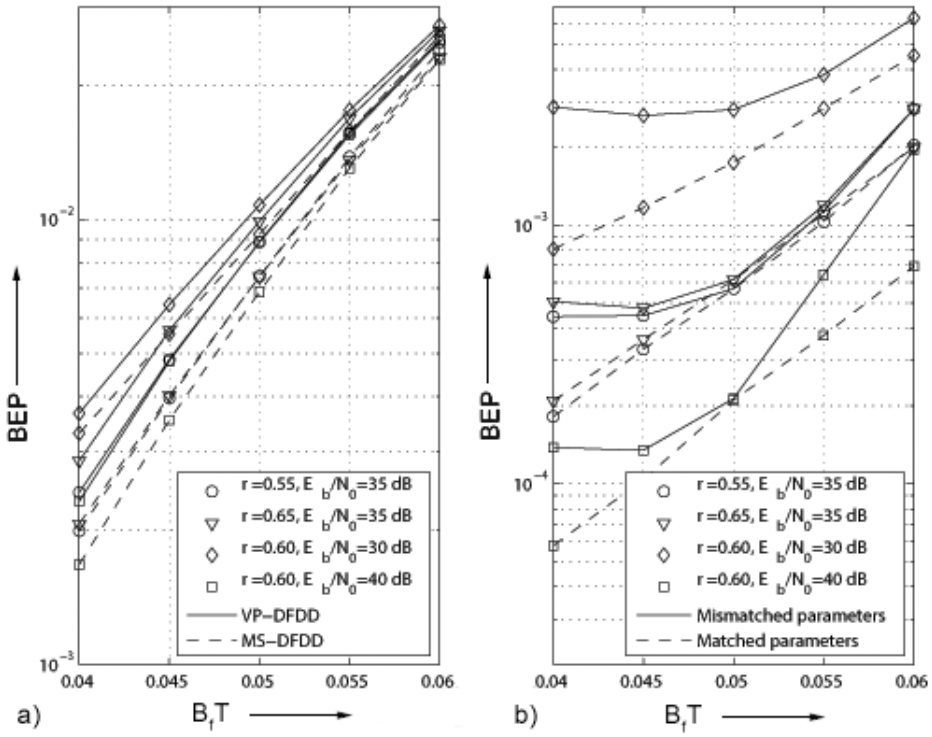

Figure 2.5: BEP vs. B_fT for diagonal DSTM with $R = 2$ bit/(channel use), $N_T = 2$, and $N_R = 1$ under various channel conditions. a) MS–DFDD (proposed) and VP–DFDD designed for $\widehat{B_fT} = 0.05$, $\hat{\rho} = 0.6$, and $\widehat{E_b/N_0} = 35$ dB; b) MS–DFDD (proposed) designed for matched and mismatched ($\widehat{B_fT} = 0.05$, $\hat{\rho} = 0.6$, and $\widehat{E_b/N_0} = 35$ dB) channel parameters.

Chapter 3

1 The Generalized K–Fading Model

In this section, a brief review of the PDF of the instantaneous received SNR for generalized K–fading is introduced. Subsequently, certain moment generating functions (MGFs) for the case of cascade multipath fading and the case of composite shadowing/multipath fading are also derived. For the remainder of this thesis, we assume quasi–static channel conditions, i.e., the instantaneous SNRs of all fading branches remain constant over an entire block of data symbols and change randomly from one block to the next.

3.1 PDF of the Instantaneous Received SNR

In order to derive the generalized K–distribution, we first consider the case of composite shadowing and multipath fading [22]. In this case, the generalized K–fading model describes a composite Gamma–shadowing/Nakagami–m fading process. The PDF of the instantaneous SNR γ, conditioned on the average SNR $\bar{\gamma}$, is given by

$$p_{\gamma|\bar{\gamma}}(\gamma|\bar{\gamma}) = \frac{m^m \gamma^{m-1}}{\Gamma(m)\bar{\gamma}^m} \exp\left(-\frac{m\gamma}{\bar{\gamma}}\right), \quad m > 0, \gamma \geq 0, \tag{3.1}$$

where $\Gamma(x)$ denotes the Gamma function. The average SNR $\bar{\gamma}$ itself is a random variable with PDF given by

$$p_{\bar{\gamma}}(\bar{\gamma}) = \frac{\bar{\gamma}^{k-1}}{\Gamma(k)\,\bar{\bar{\gamma}}^{k}} \exp\left(-\frac{\bar{\gamma}}{\bar{\bar{\gamma}}}\right), \quad k > 0, \bar{\gamma} \geq 0, \tag{3.2}$$

where $\bar{\bar{\gamma}} \triangleq \mathcal{E}\{\bar{\gamma}\}$. By combining the above two equations we obtain the PDF of the instantaneous SNR γ given by

$$p_{\gamma}(\gamma) = \frac{a^{\beta+1}}{\Gamma(k)\Gamma(m)2^{\beta}} \gamma^{\frac{\beta-1}{2}} K_{\alpha}(a\sqrt{\gamma}), \tag{3.3}$$

where $a \triangleq 2\sqrt{\frac{m}{\bar{\bar{\gamma}}}}$, $\alpha \triangleq k - m$, $\beta \triangleq k + m - 1$, and $K_v(x)$ denotes the modified Bessel function of the second kind and order v. This instantaneous SNR may also be used to model cascade multipath fading. As an example, the case of double Rayleigh–fading [9, 10] is obtained when $k = m = 1$, where

$$p_{\gamma}(\gamma) = \frac{2}{\bar{\bar{\gamma}}} K_0\left(2\sqrt{\frac{m}{\bar{\bar{\gamma}}}}\right). \tag{3.4}$$

More or less severe cascade multipath fading can be modeled by varying the parameters k and m accordingly. In particular, for the special case where $k = 1$, we obtain a cascade multipath fading model composed of a Rayleigh fading process and a Nakagami–m fading process. Finally, it is worth noting that in the case of cascade multipath fading, $\bar{\gamma}$ is a deterministic quantity and $\bar{\bar{\gamma}} = \bar{\gamma}$.

In the following, we consider transmission over L generalized K–fading branches and derive expressions for the MGF of the instantaneous sum SNR

$$\gamma_t \triangleq \sum_{l=1}^{L} \gamma_l, \tag{3.5}$$

where γ_l is the instantaneous SNR associated with the lth branch ($l \in \{1, \ldots, L\}$). These expressions will later be utilized in Section 4.3 to determine the diversity order of coherent transmission with maximum–ratio combining (MRC) at the receiver, and in Section 5 to extend our performance analysis for DBPSK/non–coherent FSK modulation with EGC at the receiver (Section 4) to the case of DQPSK and M–ary non–coherent FSK modulation. We note that the derived MGF expressions could also be useful for other performance analyses (e.g., outage analysis) and are thus of general interest.

We start with the case of independent but not necessarily identically distributed (i.n.d.) fading across branches, which is relevant for the case of cascade multipath fading. Subsequently, we address the case of composite shadowing and multipath fading.

3.2 MGF of Sum SNR for the Case of I.N.D. Fading

Let $\bar{\bar{\gamma}}_l \triangleq \mathcal{E}\{\gamma_l\}$ denote the average SNR associated with the lth branch ($l \in \{1, \ldots, L\}$). Moreover, we define $\theta \triangleq \min_{l\in\{1,\ldots,L\}}\{\bar{\bar{\gamma}}_l\}$, i.e., the average SNR $\bar{\bar{\gamma}}_l$ can be written as $\bar{\bar{\gamma}}_l \triangleq \delta_l \cdot \theta$ with constant $\delta_l \geq 1$ for all indices $l \in \{1, \ldots, L\}$. In the following, the individual branches are assumed to be characterized by independent generalized K–fading, where for the lth branch the parameters of the PDF (3.3) are given by $a_l \triangleq 2\sqrt{\frac{m_l}{\bar{\bar{\gamma}}_l}}$, $\alpha_l \triangleq k_l - m_l$, and $\beta_l \triangleq k_l + m_l - 1$.

The MGF of the instantaneous branch SNR γ_l, $\mathrm{M}_{\gamma_l}(x) \triangleq \mathcal{E}\{e^{x\gamma_l}\}$, can be derived based on (3.3) by employing [§6.643, no. 3] from [23]. Using the relation [24, Ch. 13]

$$W_{\mu,\nu}(x) = e^{-x/2}x^{\nu+1/2}U(1/2+\nu-\mu, 1+2\nu; x) \tag{3.6}$$

between the Whittaker function $W_{\mu,\nu}(x)$ and the confluent hypergeometric function of the second kind $U(a, b; x)$, one obtains the following closed-form expression:

$$\mathrm{M}_{\gamma_l}(x) = \left(\frac{-m_l}{x\delta_l\theta}\right)^{k_l} U\left(k_l, 1+\alpha_l; \frac{-m_l}{x\delta_l\theta}\right). \tag{3.7}$$

Note that $U(a, b; x)$ is also known as Kummer's function of the second kind or Tricomi's confluent hypergeometric function. In addition, for numerical evaluation, the representation [24, Ch. 13]

$$U(a,b;x) = \frac{\Gamma(1-b)}{\Gamma(a-b+1)}\,{}_1F_1(a,b;x) + x^{1-b}\frac{\Gamma(b-1)}{\Gamma(a)}\,{}_1F_1(a-b+1,2-b;x) \tag{3.8}$$

of $U(a,b;x)$ in terms of the Kummer confluent hypergeometric function ${}_1F_1(a,b;x)$ is sometimes preferable, which leads to the following expression for $\mathrm{M}_{\gamma_l}(x)$:

$$\mathrm{M}_{\gamma_l}(x) = \left(\frac{-m_l}{x\delta_l\theta}\right)^{k_l}\frac{\Gamma(-\alpha_l)}{\Gamma(m_l)}\,{}_1F_1\left(k_l,1+\alpha_l;\frac{-m}{x\delta_l\theta}\right) + \left(\frac{-m_l}{x\delta_l\theta}\right)^{m_l}\frac{\Gamma(\alpha_l)}{\Gamma(k_l)}\,{}_1F_1\left(m_l,1-\alpha_l;\frac{-m}{x\delta_l\theta}\right). \tag{3.9}$$

Due to the assumption of independent fading, the MGF of the instantaneous sum SNR γ_t according to (3.5), $\mathrm{M}_{\gamma_t}(x) \triangleq \mathcal{E}\{e^{x\gamma_t}\}$, is given by

$$\mathrm{M}_{\gamma_t}(x) = \prod_{l=1}^{L}\left(\frac{-m_l}{x\delta_l\theta}\right)^{k_l} U\left(k_l,1+\alpha_l;\frac{-m_l}{x\delta_l\theta}\right). \tag{3.10}$$

In the case of i.i.d. fading, the above expression reduces to

$$\mathrm{M}_{\gamma_t}(x) = \left(\frac{-m_l}{x\theta}\right)^{kL}\left[U\left(k,1+\alpha;\frac{-m}{x\theta}\right)\right]^{L} \tag{3.11}$$

$\Big(k_1 = \ldots = k_L \triangleq k, m_1 = \ldots = m_L \triangleq m, \delta_1 = \ldots = \delta_L \triangleq 1\Big)$.

3.3 MGF of Sum SNR for Correlated Composite Shadowing and Multipath Fading

In the case of composite shadowing and multipath fading, it is assumed that the shadowing part is fully correlated across links, whereas the multipath fading is i.i.d. across the L branches $\Big(k_1 = \ldots = k_L \triangleq k, m_1 = \ldots = m_L \triangleq m\Big)$. Correspondingly, all branches are characterized by the same average SNR, $\bar{\gamma}$, which itself is a random variable with PDF given by (3.2). Moreover, we

have $\bar{\bar{\gamma}}_1 = \ldots = \bar{\bar{\gamma}}_L \triangleq \theta$. The joint PDF of the instantaneous branch SNRs $\gamma_l \, (l \in \{1, \ldots, L\})$, conditioned on the average SNR $\bar{\gamma}$, is given by

$$p_{\gamma_1,\ldots,\gamma_L|\bar{\gamma}} \left(\gamma_1, \ldots, \gamma_L|\bar{\gamma}\right) = \prod_{l=1}^{L} p_{\gamma_l|\bar{\gamma}} \left(\gamma_l|\bar{\gamma}\right), \tag{3.12}$$

due to the assumption of independent multipath fading across the L branches. Correspondingly, the conditional MGF of the instantaneous sum SNR γ_t, $\mathrm{M}_{\gamma_t|\bar{\gamma}} \left(x\right) \triangleq \int_0^\infty e^{x\gamma_t} p_{\gamma_t|\bar{\gamma}} \left(\gamma_t|\bar{\gamma}\right) d\gamma_t$, is given by

$$\mathrm{M}_{\gamma_t|\bar{\gamma}} \left(x\right) = \prod_{l=1}^{L} \mathrm{M}_{\gamma_l|\bar{\gamma}} \left(x\right). \tag{3.13}$$

Based on (3.1) and [§3.381, no. 4] from [23], the conditional MGF of the instantaneous branch SNR γ_l, $\mathrm{M}_{\gamma_l|\bar{\gamma}} \left(x\right) \triangleq \int_0^\infty e^{x\gamma_l} p_{\gamma_l|\bar{\gamma}} \left(\gamma_l|\bar{\gamma}\right) d\gamma_l$, can be calculated as

$$\mathrm{M}_{\gamma_l|\bar{\gamma}} \left(x\right) = \left(\frac{m}{m - x\bar{\gamma}}\right)^m, \quad \Re\{x\} < 0, \tag{3.14}$$

which is the well-known MGF for Nakagami-m fading [13, Ch. 2.2]. Based on (3.2), (3.13) and (3.14), the (unconditional) MGF of γ_t can be written as

$$\mathrm{M}_{\gamma_t} \left(x\right) = \frac{1}{\Gamma\left(k\right) \theta^k} \int_0^\infty \frac{\bar{\gamma}^{k-1}}{\left(1 - \frac{x}{m}\bar{\gamma}\right)^{mL}} \cdot e^{-\bar{\gamma}/\theta} d\bar{\gamma}. \tag{3.15}$$

As will be seen in Section 5.3, error probabilities for values $m \in \mathbb{N}$, where $\mathbb{N}$ denotes the set of all integers greater than zero, can typically be evaluated with a high accuracy by replacing m with a slightly different value $m \pm \epsilon \notin \mathbb{N}$, where $\epsilon > 0$ is a small perturbation value. Therefore, assuming that m is a finite non-integer value and employing [§3.383, no. 5] from [23], we find the following closed-form expression for the MGF of γ_t:

$$\begin{aligned}\mathrm{M}_{\gamma_t}(x) &= (k)_{-mL}\cdot(mL)_{1-k} \qquad (3.16)\\ &\times\left[\left(\frac{-m}{x\,\theta}\right)^{mL}\frac{\Gamma(mL)\,\Gamma(1-mL)}{\Gamma(1-k)}\cdot L_{-mL}^{-\Delta_{k,m}}\left(\frac{-m}{x\,\theta}\right)\right.\\ &\left.-\left(\frac{-m}{x\,\theta}\right)^{k}\frac{\Gamma(k)\,\Gamma(1-k)}{\Gamma(1-mL)}\cdot L_{-k}^{\Delta_{k,m}}\left(\frac{-m}{x\,\theta}\right)\right],\quad \theta<\infty,\ \ \Re\{x\}<0.\end{aligned}$$

where $(x)_\nu \triangleq \Gamma(x+\nu)/\Gamma(x)$ denotes the Pochhammer symbol and $L_a^b(x)$ denotes the generalized Laguerre function. Moreover, the identity $\Gamma(x)\,\Gamma(1-x) = \pi/\sin(\pi x)$ is used for the Gamma function and the short-hand notation $\Delta_{k,m} \triangleq k-mL$ is introduced. Finally, similar to Section 3.2, the MGF (3.16) can be expressed in terms of the Kummer confluent hypergeometric function ${}_1F_1(a,b;x)$:

$$\begin{aligned}\mathrm{M}_{\gamma_t}(x) &= \gamma(\Delta_{k,m})\cdot\left[\left(\frac{-m}{x\theta}\right)^{mL}\frac{1}{\Gamma(k)}\,{}_1F_1\left(mL,1-\Delta_{k,m};\frac{-m}{x\theta}\right)\right. \qquad (3.17)\\ &\left.-\left(\frac{-m}{x\theta}\right)^{k}\frac{1}{\Gamma(mL)}\frac{\Gamma(1-\Delta_{k,m})}{\Gamma(1+\Delta_{k,m})}\,{}_1F_1\left(k,1+\Delta_{k,m};\frac{-m}{x\theta}\right)\right],\end{aligned}$$

where we have used the relation [24, Ch. 13]

$$L_a^b(x) = \frac{(b+1)_a}{\gamma(a+1)}\,{}_1F_1(-a,b+1;x). \qquad (3.18)$$

for non-integer values of b.

Chapter 4

1 Generalized K–Fading: Binary Modulation Scenario

In this section, closed–form BEP expressions for DBPSK/non–coherent FSK modulation over L generalized K–fading branches with EGC at the receiver are derived. We start with the case of i.n.d. fading across branches. Furthermore, we will derive the expressions for the case of composite shadowing and multipath fading.

4.1 BEP for I.N.D. Fading

In this section, we consider the case of DPSK/non–coherent FSK modulation over L branches with EGC at the receiver, the instantaneous EGC output SNR is given by $\gamma_t \triangleq \sum_{l=1}^{L} \gamma_l$ [13, Ch. 9.4], where γ_l denotes the instantaneous SNR associated with the lth branch. For a fixed value of γ_t, the BEP of DBPSK/non–coherent FSK modulation over L branches with EGC at the receiver is given by [25, Ch. 14.4]

$$P_b(\gamma_t) = \frac{1}{2^{2L-1}} \exp(-g\gamma_t) \sum_{l=0}^{L-1} c_l (g\gamma_t)^l, \tag{4.1}$$

$$c_l \triangleq \frac{1}{l!} \sum_{\kappa=0}^{L-1-l} \binom{2L-1}{\kappa}, \tag{4.2}$$

where $g \triangleq 1$ for DBPSK and $g \triangleq 1/2$ for binary non–coherent FSK modulation. In order to derive a closed–form expression for the average BEP $\bar{P}_b(\theta) \triangleq \mathcal{E}_{\gamma t}\{P_b(\gamma_t)\}$, we first note that the joint PDF of the instantaneous branch SNRs $\gamma_l\,(l \in \{1,\ldots,L\})$ is given by

$$p_{\gamma_1,\ldots,\gamma_L}(\gamma_1,\ldots,\gamma_L) = \prod_{l=1}^{L} p_{\gamma_l}(\gamma_l), \tag{4.3}$$

due to the assumption of independent fading across the L branches. Furthermore, we define the index vector $\boldsymbol{\kappa} \triangleq [\kappa_1,\ldots,\kappa_L] \in \mathbb{N}_0^L$ and the index set

$$\mathbb{K}_l \triangleq \left\{\boldsymbol{\kappa} \in \mathbb{N}_0^L \mid \kappa_1 + \ldots + \kappa_L = l\right\}, \tag{4.4}$$

where $\mathbb{N}_0$ denotes the set of all integers greater than or equal to zero. We also note that γ_t^l can be expressed as [24, Ch. 24]

$$\gamma_t^l = (\gamma_1 + \ldots + \gamma_L)^l = \sum_{\boldsymbol{\kappa}\in\mathbb{K}_l} \binom{l}{\boldsymbol{\kappa}} \gamma_1^{\kappa_1} \ldots \gamma_L^{\kappa_L}, \tag{4.5}$$

where $\binom{l}{\boldsymbol{\kappa}} \triangleq l!/(\kappa_1!\ldots\kappa_L!)$. Based on the above findings, the average BEP $\bar{P}_b(\theta)$ can be expressed as

$$\bar{P}_b(\theta) = \frac{1}{2^{2L-1}} \sum_{l=0}^{L-1} c_l g^l \sum_{\boldsymbol{\kappa}\in\mathbb{K}_l} \binom{l}{\boldsymbol{\kappa}} \left(\prod_{\lambda=1}^{L} \int_0^\infty \exp(-g\gamma_\lambda) \gamma_\lambda^{\kappa_\lambda} p_{\gamma_\lambda}(\gamma_\lambda)\, d\gamma_\lambda \right). \tag{4.6}$$

Plugging in (3.3) for the PDFs $p_{\gamma_l}(\gamma_l)$, $l \in \{1,\ldots,L\}$, and employing [§6.643, no. 3] from [23] in conjunction with (3.6), we obtain for the average BEP the following closed–form expression:

$$\begin{aligned} \bar{P}_b(\theta) &= \frac{1}{2^{2L-1}} \sum_{l=0}^{L-1} c_l \sum_{\boldsymbol{\kappa}\in\mathbb{K}_l} \binom{l}{\boldsymbol{\kappa}} \\ &\quad \times \left(\prod_{\lambda=1}^{L} \frac{(k_\lambda)_{\kappa_\lambda} (m_\lambda)_{\kappa_\lambda}}{g^{k_\lambda}} \left(\frac{m_\lambda}{\delta_\lambda \theta}\right)^{k_\lambda} U\left(k_\lambda + \kappa_\lambda, 1 + \alpha_\lambda; \frac{m_\lambda}{g\delta_\lambda\theta}\right) \right). \end{aligned} \tag{4.7}$$

For the special case of i.i.d. fading, where $k_1 = \ldots = k_L \triangleq k$, $m_1 = \ldots = m_L \triangleq m$, $\alpha \triangleq k - m$, and $\delta_1 = \ldots = \delta_L \triangleq 1$, (4.7) simplifies to

$$\begin{aligned} \bar{P}_b(\theta) &= \frac{1}{2^{2L-1}} \left(\frac{m}{g\theta}\right)^{kL} \sum_{l=0}^{L-1} c_l \sum_{\boldsymbol{\kappa}\in\mathbb{K}_l} \binom{l}{\boldsymbol{\kappa}} \\ &\quad \times \left(\prod_{\lambda=1}^{L} (k)_{\kappa_\lambda} (m)_{\kappa_\lambda} U\left(k + \kappa_\lambda, 1 + \alpha; \frac{m}{g\theta}\right) \right). \end{aligned} \tag{4.8}$$

Finally, for the special case $L = 1$, (4.1) reduces to $P_b(\gamma_t) = P_b(\gamma_1) = \frac{1}{2}e^{-g\gamma_1}$, and $\bar{P}_b(\theta)$ can be evaluated as

$$\bar{P}_b(\theta) = \frac{1}{2}\left(\frac{m}{g\theta}\right)^k U\left(k, 1+\alpha; \frac{m}{g\theta}\right). \tag{4.9}$$

For comparison, in the case of i.i.d. Rayleigh fading the average BEP $\bar{P}_b(\theta)$ is given by [25, Ch. 14.4]

$$\bar{P}_b(\theta) = \frac{1}{2^{2L-1}(L-1)!(1+g\theta)^L}\sum_{l=0}^{L-1} c_l (L-1+l)!\left(\frac{g\theta}{1+g\theta}\right)^l, \tag{4.10}$$

and we have

$$\bar{P}_b(\theta) = \frac{1}{2(1+g\theta)}, \tag{4.11}$$

for the special case $L = 1$.

4.2 BEP for Correlated Composite Shadowing and Multipath Fading

In the case of composite shadowing and multipath fading, we again assume that the shadowing part is fully correlated across links, whereas the multipath fading is i.i.d. across the L branches. In or to arrive at a closed–form expression for the average BEP $\bar{P}_b(\theta)$, we first average (4.1) over the instantaneous branch SNRs γ_l, while conditioning on $\bar{\gamma}$. In the final step, the resulting conditional BEP, denoted as $\bar{P}_b(\bar{\gamma})$, is then averaged over $\bar{\gamma}$.

Similar to (4.6), the conditional BEP $\bar{P}_b(\bar{\gamma})$ can be written as

$$\bar{P}_b(\bar{\gamma}) = \frac{1}{2^{2L-1}}\sum_{l=0}^{L-1} c_l g^l \sum_{\boldsymbol{\kappa}\in\mathbb{K}_l}\binom{l}{\boldsymbol{\kappa}}\left(\prod_{\lambda=1}^{L}\int_0^\infty e^{-g\gamma_\lambda}\gamma_\lambda^{\kappa_\lambda} p_{\gamma_\lambda|\bar{\gamma}}(\gamma_\lambda|\bar{\gamma})\, d\gamma_\lambda\right), \tag{4.12}$$

where we have used the joint PDF $p_{\gamma_1,\ldots,\gamma_L|\bar{\gamma}}(\gamma_1,\ldots,\gamma_L|\bar{\gamma})$, conditioned on the average SNR $\bar{\gamma}$, can be written as the product of the conditional PDFs

$p_{\gamma_l|\bar{\gamma}}(\gamma_l|\bar{\gamma})$ of the instantaneous branch SNRs $\gamma_l\,(l \in \{1,\ldots,L\})$, cf. (3.12). Plugging in (3.1) for the conditional PDFs $p_{\gamma_l|\bar{\gamma}}(\gamma_l|\bar{\gamma})$ and employing [§3.381, no.4] from [23], we find the following expression for $\bar{P}_b(\bar{\gamma})$:

$$\begin{aligned}\bar{P}_b(\bar{\gamma}) &= \frac{1}{2^{2L-1}}\left(\frac{m^m}{\Gamma(m)}\right)^L \sum_{l=0}^{L-1} c_l g^l \sum_{\boldsymbol{\kappa}\in\mathbb{K}_l}\binom{l}{\boldsymbol{\kappa}} \\ &\quad\times\left(\prod_{\lambda=1}^{L}\Gamma(m+\kappa_\lambda)\,\frac{\bar{\gamma}^{\bar{\kappa}_\lambda}}{(g\bar{\gamma}+m)^{m+\kappa_\lambda}}\right),\end{aligned} \tag{4.13}$$

$\Big(m_1 = \ldots = m_L \triangleq m\Big)$. Based on the PDF (3.2) of the average SNR $\bar{\gamma}$, the average BEP $\bar{P}_b\left(\bar{\theta}\right) \triangleq \mathcal{E}_{\bar{\gamma}}\{\bar{P}_b(\bar{\gamma})\}$ can be written as

$$\begin{aligned}\bar{P}_b\left(\bar{\theta}\right) &= \frac{1}{2^{2L-1}}\,\frac{1}{\Gamma(k)\left(\Gamma(m)\right)^L\theta^k}\sum_{l=0}^{L-1} c_l g^l \\ &\quad\times\sum_{\boldsymbol{\kappa}\in\mathbb{K}_l}\binom{l}{\boldsymbol{\kappa}}\frac{\prod_{\lambda=1}^{L}\Gamma(m+\kappa_\lambda)}{m^l}\int_0^\infty \frac{\bar{\gamma}^{k+l-1}\cdot e^{-\bar{\gamma}/\theta}}{\left(\frac{g}{m}\bar{\gamma}+1\right)^{mL+l}}\,d\bar{\gamma}.\end{aligned} \tag{4.14}$$

Employing [§3.383, no. 5] from [23] and assuming that m is a finite non-integer value and $k \neq mL$, we find the following closed–form expression for the average BEP $\bar{P}_b(\theta)$:

$$\begin{aligned}\bar{P}_b(\theta) &= \frac{1}{2^{2L-1}}\,\frac{1}{\Gamma(k)}\,\frac{\pi}{\sin(\pi\Delta_{k,m})} \\ &\quad\times\sum_{l=0}^{L-1} c_l\left[\sum_{\boldsymbol{\kappa}\in\mathbb{K}_l}\binom{l}{\boldsymbol{\kappa}}\left(\prod_{\lambda=1}^{L}(m)_{\kappa_\lambda}\right)\right] \\ &\quad\times\left[\left(\frac{m}{g\theta}\right)^{mL}\frac{\Gamma(1-\varphi_{m,l})}{\Gamma(1-\psi_{k,l})}L_{-\varphi_{m,l}}^{-\Delta_{k,m}}\left(\frac{m}{g\theta}\right)\right. \\ &\quad\left.-\left(\frac{m}{g\theta}\right)^{k}\frac{\sin(\pi\varphi_{m,l})}{\sin(\pi\psi_{k,l})}L_{-\psi_{k,l}}^{\Delta_{k,m}}\left(\frac{m}{g\theta}\right)\right],\end{aligned} \tag{4.15}$$

where we have introduced the short–hand notations $\psi_{k,l} \triangleq k+l$ and $\varphi_{m,l} \triangleq mL+l$.

4.3 Asymptotic Analysis and Diversity Order

Since the closed–form BEP expressions (4.8) and (4.12) involve non–standard functions and the primary behavior of the resulting BEP curves is not obvious, in this section, we will investigate the behavior of (4.8) and (4.12) for high SNR values ($\theta \to \infty$). In particular, we derive expressions for the resulting (asymptotic) diversity order[1].

$$d \triangleq \lim_{\theta \to \infty} d(\theta), \quad d(\theta) \triangleq -\frac{\partial \log\left(\bar{P}_b(\theta)\right)}{\partial \log(\theta)}. \tag{4.16}$$

In particular, we show that the diversity order of DBPSK/non-coherent FSK modulation is, in fact, the same as that in the case of coherent transmission.

4.3.1 The Case of Independent Fading

For the ease of exposition, we focus on the case of i.i.d. fading here, i.e., $\bar{\bar{\gamma}}_1 = \ldots = \bar{\bar{\gamma}}_L = \theta$, $m_1 = \ldots = m_L \triangleq m$, $k_1 = \ldots = k_L \triangleq k$. An extension to the case of i.n.d fading is, however, straightforward. In the following, we derive approximate expressions for the average BEP (4.9), by employing corresponding approximations of the confluent hypergeometric function $U(a, b; x)$.

Consider first the case where the two fading parameters k and m are different, i.e., $\alpha = k - m \neq 0$. For the ease of exposition, we assume that α is a non–integer value. For $x \to \infty$ and non–integer values of b, the confluent hypergeometric function $U(a, b; x)$ can be approximated as [24, Ch. 13]

$$U(a, b; x) \doteq \frac{\Gamma(1-b)}{\Gamma(1-b+a)} + \frac{\Gamma(b-1)}{\Gamma(a)} x^{1-b}, \tag{4.17}$$

[1]The (asymptotic) diversity order is the negative slope of the BEP curve for high SNR values on a log–log scale. It has been shown to be a useful measure for characterizing the principal behavior of digital transmission schemes over various fading channels [25, Ch. 14.4].

where $\doteq$ denotes asymptotic equality. For $\theta \to \infty$ and non–integer values of α, the average BEP (4.8) can thus be approximated as

$$\bar{P}_b(\theta) \doteq \frac{1}{2^{2L-1}} \left(\frac{m}{g\theta}\right)^{\xi_1 L} \sum_{l=0}^{L-1} c_l \sum_{\boldsymbol{\kappa} \in \mathbb{K}_l} \binom{l}{\boldsymbol{\kappa}} \left(\prod_{\lambda=1}^{L} \frac{(k)_{\kappa_\lambda} (m)_{\kappa_\lambda} \Gamma(|\alpha|)}{\Gamma(k+\kappa_\lambda)\Gamma(\xi_2+\kappa_\lambda)} \right). \quad (4.18)$$

where $\xi_1 \triangleq \min\{k, m\}$ and $\xi_2 \triangleq \max\{k, m\}$. In the case $k < m$, (4.18) simplifies to

$$\bar{P}_b(\theta) \doteq \frac{1}{2^{2L-1}} \left(\frac{m}{g\theta}\right)^{\xi_1 L} \left(\frac{\Gamma(|\alpha|)}{\Gamma(k)\Gamma(m)}\right)^{L} \sum_{l=0}^{L-1} c_l \sum_{\boldsymbol{\kappa} \in \mathbb{K}_l} \binom{l}{\boldsymbol{\kappa}}. \quad (4.19)$$

From (4.18) and (4.19) we find

$$d = \xi_1 L = \min\{k, m\} \cdot L. \quad (4.20)$$

Interestingly, the smaller of the two fading parameters, k and m, limits the asymptotic diversity order. For example, in the case of cascade Rayleigh/ Nakagami–m fading with $k = 1$ and $m \geq 1$ the asymptotic diversity order is always given by $d = L$, just as in the case of pure Rayleigh fading, where [25, Ch. 14.4]

$$\bar{P}_b(\theta) \doteq \left(\frac{1}{2g\theta}\right)^{L} \binom{2L-1}{L}. \quad (4.21)$$

Next, consider the case $\alpha = 0$, i.e., $k = m$. For $x \to 0$ and $b = 1$, the confluent hypergeometric function $U(a, b; x)$ can be approximated as [24, Ch. 13]

$$U(a, b; x) \doteq -\frac{1}{\Gamma(a)} \left(\ln(x) + \Psi(a) + 2\gamma'\right), \quad (4.22)$$

where $\Psi(x) \triangleq \left(\frac{\partial}{\partial x}\Gamma(x)\right)/\Gamma(x)$ denotes the Digamma function and γ' the Euler–Mascheroni constant. For $\theta \to \infty$ and $\alpha = 0$, the average BEP (4.9) can thus be approximated as

$$\bar{P}_b(\theta) \doteq \frac{1}{2^{2L-1}} \left[-\left(\frac{m}{g\theta}\right)^k \ln\left(\frac{m}{g\theta}\right) \right]^L \times \sum_{l=0}^{L-1} c_l \sum_{\boldsymbol{\kappa}\in\mathbb{K}_l} \binom{l}{\boldsymbol{\kappa}} \left(\prod_{\lambda=1}^{L} \frac{(k)_{\kappa_\lambda} (m)_{\kappa_\lambda}}{\Gamma(k+\kappa_\lambda)} \right). \tag{4.23}$$

Correspondingly, we find

$$d(\theta) = \left(k - \frac{1}{\ln(\theta)}\right) L = \left(m - \frac{1}{\ln(\theta)}\right) L, \tag{4.24}$$

i.e., the asymptotic diversity order is given by

$$d = kL = mL. \tag{4.25}$$

This result is in accordance with [10], where the diversity order of various coherent modulation schemes was determined for the special case of a single branch ($L = 1$) being subject to double Rayleigh fading ($k = m = 1$). Moreover, note that (4.25) is also in accordance with (4.20).

Finally, we compare the above results for DBPSK/non–coherent FSK modulation to the asymptotic diversity order obtained in the case of a coherent transmission scheme. As an example, we consider a binary phase shift keying (BPSK) scheme over L i.i.d. generalized K–fading links with MRC at the receiver. The corresponding average BEP can be determined via the following finite–range integral [26]:

$$\bar{P}_b(\theta) = \frac{1}{\pi} \int_0^{\pi/2} \mathrm{M}_{\gamma_t}\left(-\frac{1}{\sin^2(\phi)}\right) d\phi, \tag{4.26}$$

where the MGF $\mathrm{M}_{\gamma t}(x)$ of the instantaneous MRC output SNR $\gamma_t = \sum_{l=1}^{L} \gamma_l$ is given by (3.11). As earlier, we assume for simplicity that α is a non–integer value. Based on (4.17) and employing [§3.621, no. 1] from [23], the average BEP (4.26) for high SNR values $\theta \to \infty$ can be approximated as

$$\bar{P}_b(\theta) \doteq \frac{1}{2\pi} \left(\frac{\Gamma(|\alpha|)}{\Gamma(\xi_2)}\right)^L \left(\frac{4m}{\theta}\right)^{\xi_1 L} B(\xi_1 L + 1/2, \xi_1 L + 1/2), \tag{4.27}$$

where $B(x,y)$ denotes the Beta function. Correspondingly, the diversity order of BPSK modulation over L i.i.d. generalized K–fading links with MRC at the receiver is given by

$$d = \xi_1 L = \min\{k,m\} \cdot L, \tag{4.28}$$

just as in the case of the considered non–coherent transmission schemes, cf. (4.20).

4.3.2 Correlated Composite Shadowing and Multipath Fading

In this section, we derive an approximate expression for the average BEP (4.15) for high SNR values $\theta \to \infty$, by employing a corresponding approximation of the generalized Laguerre function $L_a^b(x)$. For $x \to \infty$, the generalized Laguerre function $L_a^b(x)$ can be approximated as [27, Ch. 13.2]

$$L_a^b(x) \doteq \frac{(b+1)_a}{\Gamma(a+1)}. \tag{4.29}$$

For $\theta \to \infty$, the average BEP (4.15) can thus be approximated as

$$\begin{aligned} \bar{P}_{\mathrm{b}}(\theta) \;\doteq\; & \frac{1}{2^{2L-1}} \frac{\operatorname{sign}(\Delta_{k,m})}{\Gamma(k)} \frac{\pi}{\sin(\pi\Delta_{k,m})} \left(\frac{m}{g\theta}\right)^{\zeta_1} \sum_{l=0}^{L-1} c_l \Xi_l \\ & \times \left[\sum_{\boldsymbol{\kappa}\in\mathbb{K}_l} \binom{l}{\boldsymbol{\kappa}} \left(\prod_{\lambda=1}^{L} (m)_{\kappa_\lambda}\right)\right] \frac{(1-|\Delta_{k,m}|)_{-\zeta_1-l}}{\Gamma(1-\psi_{k,l})}, \end{aligned} \tag{4.30}$$

where $\zeta_1 \triangleq \min\{k, mL\}$, $\operatorname{sign}(x)$ denotes the sign function (i.e., $\operatorname{sign}(x)$=+1 for all $x \geq 0$ and $\operatorname{sign}(x)$= -1 otherwise), and[2]

[2]As earlier, we assume that $k \neq mL$, since otherwise (4.15) is not valid. However, it turns out that (4.30) yields nearly identical results for $k = mL + \epsilon$ and $k = mL - \epsilon$, if ϵ is chosen sufficiently small.

$$\Xi_l \triangleq \begin{cases} \sin(\pi\varphi_{m,l})/\sin(\pi\psi_{k,l}) & \text{for } k<mL \\ 1 & \text{for } k>mL \end{cases} . \tag{4.31}$$

Correspondingly, the asymptotic diversity order in the case of correlated composite shadowing and multipath fading is obtained as

$$d = \zeta_1 = \min\{k, mL\}. \tag{4.32}$$

This result reveals an interesting interplay between macroscopic diversity due to shadowing effects and microscopic diversity due to multipath fading: the asymptotic diversity order is always limited by either the shadowing effect ($k \leq mL$) or the multipath fading ($mL < k$), depending on which one of the two fading effects is more severe.

In order to arrive at (4.30) , we have utilized that for $\theta \to \infty$ only one of the two $L_a^b(x)$–terms in (4.15) dominates, namely the one which is associated with the term $(\frac{m}{g\,\theta})^{\zeta_1}$. Correspondingly, if $k \approx mL$ the convergence of the asymptotic solution (4.30) to the exact expression (4.15) can be expected to be rather slow, since the dominant term will only emerge for very large values of θ. However, if k and mL are sufficiently different, the convergence of (4.30) is typically quite fast, as will be seen from the numerical performance results presented in Section 5.3.

In order to compare the asymptotic diversity order (4.32) for DBPSK/non–coherent FSK modulation to that in the case of BPSK modulation, we first note that (4.26) is valid for arbitrary fading correlations (if an expression for the MGF $\mathrm{M}_{\gamma_t}(x)$ of the instantaneous MRC output SNR γ_t is available). In the case of correlated composite shadowing and multipath fading, the MGF $\mathrm{M}_{\gamma_t}(x)$ is given by (3.16). Based on (4.29) and employing [§3.621, no. 1] from [23], the average BEP (4.26) for $\theta \to \infty$ can be approximated as

$$\bar{P}_{\mathrm{b}}(\theta) \doteq \frac{\operatorname{sign}(\Delta_{k,m})(k)_{-mL}(mL)_{1-k}}{2\pi} \times \frac{\Gamma(\zeta_1)(1-|\Delta_{k,m}|)_{-\zeta_1}}{\Gamma(1-\zeta_2)} \left(\frac{4m}{\theta}\right)^{\zeta_1} B(\zeta_1+1/2, \zeta_1+1/2), \tag{4.33}$$

where $\zeta_2 \triangleq \max\{k, mL\}$. Correspondingly, the diversity order of BPSK modulation over L correlated composite shadowing/multipath fading links with MRC at the receiver is given by

$$d = \zeta_1 = \min\{k, mL\}, \tag{4.34}$$

just as in the case of the non–coherent transmission schemes, cf. (4.32).

Chapter 5

1 Generalized K–Fading: Extensions to M–ary Modulation

The closed-form expressions (3.10) and (3.16) for the MGF of the instantaneous sum SNR γ_t in the case of i.n.d. fading and correlated composite shadowing/multipath fading, respectively, can be utilized to extend our performance analysis in Section 4 to the case of non–binary transmission. As an example, we will focus on the average BEP of DQPSK modulation with Gray mapping, the average BEP of M–ary orthogonal FSK modulation, and the average symbol error probability (SEP) of coherent M–ary phase shift keying (PSK) modulation.

5.1 BEP for I.N.D. Fading

In the case of i.n.d. fading, the average BEP of DQPSK modulation with Gray mapping over L branches with EGC at the receiver is given by [13, Ch. 9.4]

$$\bar{P}_b(\theta) = \frac{1}{\pi 2^{2L}} \int_{-\pi}^{\pi} \frac{f(L,\rho;\phi)}{1+2\rho\sin(\phi)+\rho^2} \prod_{l=1}^{L} \mathrm{M}_{\gamma_l}\left(-2-\sqrt{2}\sin(\phi)\right) d\phi, \quad (5.1)$$

where

$$f\left(L,\rho;\phi\right) \triangleq \sum_{l=1}^{L} c_l' \cdot \left[a_1\left(\rho\right)\cos\left(\left(l-1\right)\left(\phi+\pi/2\right)\right)\right. \\ \left. - \; a_2\left(\rho\right)\cos\left(l\left(\phi+\pi/2\right)\right)\right], \tag{5.2}$$

$$c_l' \triangleq \binom{2L-1}{L-l}, \;\; a_1\left(\rho\right) \triangleq \rho^{-l+1} - \rho^{l+1}, \;\; a_2\left(\rho\right) \triangleq \rho^{-l+2} - \rho^{l}, \tag{5.3}$$

$$\rho \triangleq \sqrt{\frac{2-\sqrt{2}}{2+\sqrt{2}}}, \tag{5.4}$$

and $\mathrm{M}_{\gamma_l}(x)$ is given by (3.7). Thus, the average BEP (5.1) for the case of i.n.d. generalized K–fading can be evaluated numerically via a single finite–range integral over known functions. Similarly, the average BEP for M–ary orthogonal FSK over L branches with non–coherent detection and EGC at the receiver can be evaluated numerically based on the single finite–range integral expression (9.130) in [13, Ch. 9.4], which again depends on the product of the MGFs $\mathrm{M}_{\gamma_l}(x)$, $l \in \{1,\ldots,L\}$. Finally, the average SEP for coherent M–ary PSK modulation over L branches with MRC at the receiver can be calculated via the finite–range integral[1] [26]

$$\bar{P}_{\mathrm{S}}\left(\theta\right) = \frac{1}{\pi}\int_0^{(M-1)\pi/M} \prod_{l=1}^{L} \mathrm{M}_{\gamma_l}\left(-\frac{\sin^2\left(\pi/M\right)}{\sin^2\left(\phi\right)}\right) d\phi. \tag{5.5}$$

For the special case $L=1$, there is also a finite–range integral expression for the average SEP of M–ary DPSK modulation [13, Ch. 8.2.5]:

$$\bar{P}_{\mathrm{S}}\left(\theta\right) = \frac{1}{\pi}\int_0^{(M-1)\pi/M} \mathrm{M}_{\gamma_t}\left(-\frac{\sin^2\left(\pi/M\right)}{1+\sqrt{1-\sin^2\left(\pi/M\right)}\cos\left(\phi\right)}\right) d\phi. \tag{5.6}$$

Next, we consider the case of correlated composite shadowing and multipath fading.

[1]Similar expressions can also be stated for M–ary amplitude–shift–keying (ASK) modulation and M–ary quadrature–amplitude modulation (QAM) [26].

5.2 BEP for Correlated Composite Shadowing and Multipath Fading

Since (5.1) is also valid for the case of fully correlated shadowing/i.i.d. multipath fading (proof is given at the end of the section), we have

$$\bar{P}_b(\theta) = \frac{1}{\pi 2^{2L}} \int_{-\pi}^{\pi} \frac{f(L,\rho;\phi)}{1+2\rho\sin(\phi)+\rho^2} \mathrm{M}_{\gamma_t}\left(-2-\sqrt{2}\sin(\phi)\right) d\phi, \tag{5.7}$$

where $\mathrm{M}_{\gamma_t}(x)$ is given by (3.16) .[2] Similarly, (5.5) again holds for arbitrary fading correlations, i.e., we have

$$\bar{P}_{\mathrm{S}}(\theta) = \frac{1}{\pi} \int_0^{(M-1)\pi/M} \mathrm{M}_{\gamma_t}\left(-\frac{\sin^2(\pi/M)}{\sin^2(\phi)}\right) d\phi. \tag{5.8}$$

Based on (3.16) , the average SEP (5.8) for correlated composite shadowing and multipath fading can thus be evaluated numerically via a single finite–range integral over known functions.

To prove the validity of (5.7) for the case of fully correlated shadowing/i.i.d. multipath fading, we extend the derivation of (5.1) presented in [13, Ch. 9.4] accordingly. Given a fixed value of the instantaneous EGC output SNR γ_t, the BEP of DQPSK modulation with Gray mapping over L branches with EGC at the receiver can be written as

$$\begin{aligned} \bar{P}_b(\gamma_t) &= \frac{1}{\pi 2^{2L}} \int_{-\pi}^{\pi} \frac{f(L,\rho;\phi)}{1+2\rho\sin(\phi)+\rho^2} \\ &\quad \times \prod_{l=1}^{L} \exp\left(-\frac{b^2\gamma_l}{2}\left(1+2\rho\sin(\phi)+\rho^2\right)\right) d\phi, \end{aligned} \tag{5.9}$$

where $f(L,\rho;\phi)$ and ρ are given by (5.2) and (5.4), respectively, and $b \triangleq \sqrt{2+\sqrt{2}}$ [13, Ch. 9.4]. The average BEP $\bar{P}_b(\theta)$ can thus be written as

$$\bar{P}_b(\theta) = \int_0^{\infty} \cdots \int_0^{\infty} \bar{P}_b(\gamma_t) \int_0^{\infty} \prod_{l=1}^{L} p_{\gamma_l|\bar{\gamma}}(\gamma_l|\bar{\gamma})\, p_{\bar{\gamma}}(\bar{\gamma})\, d\bar{\gamma} d\gamma_1 \cdots \gamma_L, \tag{5.10}$$

[2] Note that (5.7) is not valid for arbitrary fading correlations.

where we have used that the joint PDF $p_{\gamma_1 \cdots \gamma_L|\bar{\gamma}}(\gamma_1 \cdots \gamma_L|\bar{\gamma})$, conditioned on the average SNR $\bar{\gamma}$, can be written as the product of the conditional PDFs $p_{\gamma_l|\bar{\gamma}}(\gamma_l|\bar{\gamma})$ of the instantaneous branch SNRs $\gamma_l\,(l \in \{1,\ldots,L\})$, cf. (3.12). Using (5.8) one obtains

$$\begin{aligned}
\bar{P}_b(\theta) &= \frac{1}{\pi 2^{2L}} \int_{-\pi}^{\pi} \frac{f(L,\rho;\phi)}{1+2\rho\sin(\phi)+\rho^2} \\
&\quad \times \int_0^{\infty} \left[\prod_{l=1}^{L} \int_0^{\infty} \exp\left(-\frac{b^2\gamma_l}{2}\left(1+2\rho\sin(\phi)+\rho^2\right)\right) \right. \\
&\quad \left. \times\, p_{\gamma_l|\bar{\gamma}}(\gamma_l|\bar{\gamma})\, d\gamma_l \right] p_{\bar{\gamma}}(\bar{\gamma})\; d\bar{\gamma}\, d\phi \\
&= \frac{1}{\pi 2^{2L}} \int_{-\pi}^{\pi} \frac{f(L,\rho;\phi)}{1+2\rho\sin(\phi)+\rho^2} \\
&\quad \times \int_0^{\infty} \left[\mathrm{M}_{\gamma_l|\bar{\gamma}}\left(-\frac{b^2}{2}\left(1+2\rho\sin(\phi)+\rho^2\right)\right)\right]^L p_{\bar{\gamma}}(\bar{\gamma})\, d\bar{\gamma} d\phi \\
&= \frac{1}{\pi 2^{2L}} \int_{-\pi}^{\pi} \frac{f(L,\rho;\phi)}{1+2\rho\sin(\phi)+\rho^2} \mathrm{M}_{\gamma_t}\left(-\frac{b^2}{2}\left(1+2\rho\sin(\phi)+\rho^2\right)\right) d\phi
\end{aligned} \tag{5.11}$$

where we have used that the multipath fading is i.i.d., i.e., the conditional MGFs $\mathrm{M}_{\gamma_l|\bar{\gamma}}(x)$ are identical for all branches $l \in \{1,\ldots,L\}$ and the (unconditional) MGF $\mathrm{M}_{\gamma_t}(x)$ is given by $\mathrm{M}_{\gamma_t}(x) = \int_0^{\infty} \left[\mathrm{M}_{\gamma_l|\bar{\gamma}}(x)\right]^L p_{\bar{\gamma}}(\bar{\gamma})\, d\bar{\gamma}$. Combining (5.11) with the values for ρ and b, we finally arrives at (5.7).

5.3 Simulation and Numerical Results

In the following, numerical performance results are presented which illustrate our findings in Section 4 and Section 5. In particular, we will present Monte–Carlo simulation results, so as to corroborate our analytical performance results.

5.3.1 The Case of Independent Fading

In this section, we investigate the BEP performance of DBPSK modulation over L independent generalized K–fading branches with EGC at the receiver

(cf. Section 4.1 and 4.3.1). As an example, we focus on the case of i.i.d. cascade Rayleigh/Nakagami–m fading with $k = 1$ and $m \geq 1$.

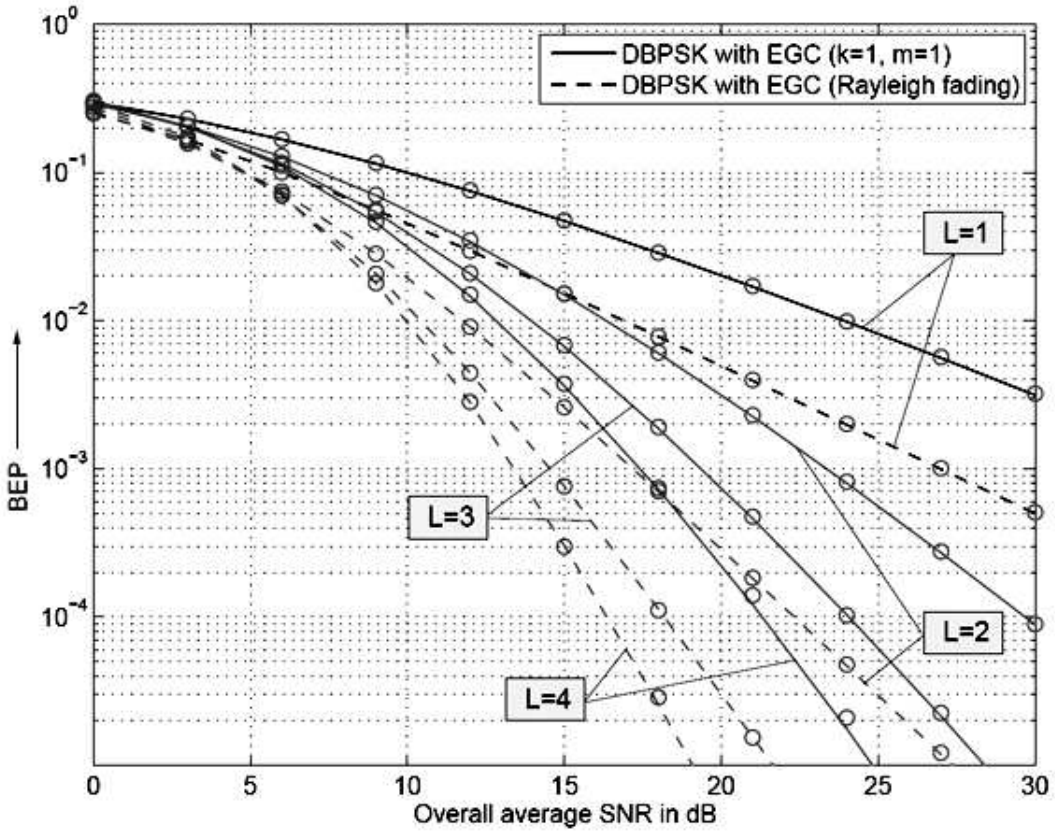

Figure 5.1: Average BEP $\bar{P}_b(\theta)$ versus average SNR $L\theta$ in dB for the case of i.i.d. double Rayleigh fading ($k = 1, m = 1$). Solid lines represent analytical results for DBPSK modulation with EGC at the receiver evaluated based on (4.8) /(4.9) using the values $k = 1.01$ and $m = 0.99$. Dashed lines represent corresponding analytical results for the case of i.i.d. Rayleigh fading evaluated based on (4.10)/(4.11). Corresponding simulation results for Rayleigh fading and double Rayleigh fading ($k = 1, m = 1$) are indicated by markers '$\circ$'.

Fig. 5.1 shows the average BEP $\bar{P}_b(\theta)$ for DBPSK versus the overall average received SNR $L\theta$ in dB for the case of i.i.d. double Rayleigh fading ($k = 1, m = 1$). The solid lines represent analytical results for $L \in \{1, \ldots, 4\}$ evaluated based on (4.8) and (4.9) using the values $k = 1.01$ and $m = 0.99$. Corresponding simulation results (for $k = 1$ and $m = 1$), obtained by Monte–

Carlo simulations over a large number of independent channel realizations, are indicated by markers '$\circ$'. As a reference, we have also included corresponding performance results for i.i.d. Rayleigh fading ($L \in \{1, \ldots, 4\}$). As can be seen, the relative performance gains obtained for $L > 1$ diversity branches are quite similar for double Rayleigh fading and conventional Rayleigh fading. However, in comparison the BEP performance for double Rayleigh fading is significantly worse than that for Rayleigh fading (for all values of L).[3] For example, in the case of $L = 4$ diversity branches, the performance difference between double Rayleigh fading and conventional Rayleigh fading at a BEP of 10^{-4} is about 5.3 dB. Vice versa, in order to achieve a BEP of less than 3×10^{-4} at an overall SNR of 20 dB, one requires $L = 4$ diversity branches in the case of double Rayleigh fading, whereas in the case of conventional Rayleigh fading $L = 2$ diversity branches are sufficient. Finally, we note that the analytical results and the simulation results are in good agreement, which corroborates our analysis in Section 4.1.

In Fig. 5.2, the average $\bar{P}_b(\theta)$ of DBPSK modulation with EGC at the receiver is compared to that of coherent BPSK modulation with MRC at the receiver. As an example, we consider again the case of i.i.d. double Rayleigh fading ($k = 1, m = 1$). The analytical curves for BPSK modulation were obtained based on (3.11) and (4.26) using numerical integration. As can be seen, the general behavior of the curves for growing values of L is quite similar in the case of DBPSK and BPSK modulation. In particular, the asymptotic slopes of the curves are identical in both cases, as predicted by our asymptotic analysis in Section 4.3.1. Interestingly, the performance difference between DBPSK and BPSK modulation at high SNR values is about 3.8 dB (for all values of L), which is slightly larger than the well–known 3 dB difference in the case of conventional Rayleigh fading.

Finally, Fig. 5.3 compares the average BEP $\bar{P}_b(\theta)$ of DBPSK with EGC

[3]For the special case $L = 1$ and coherent PSK modulation, this observation was already made in [10].

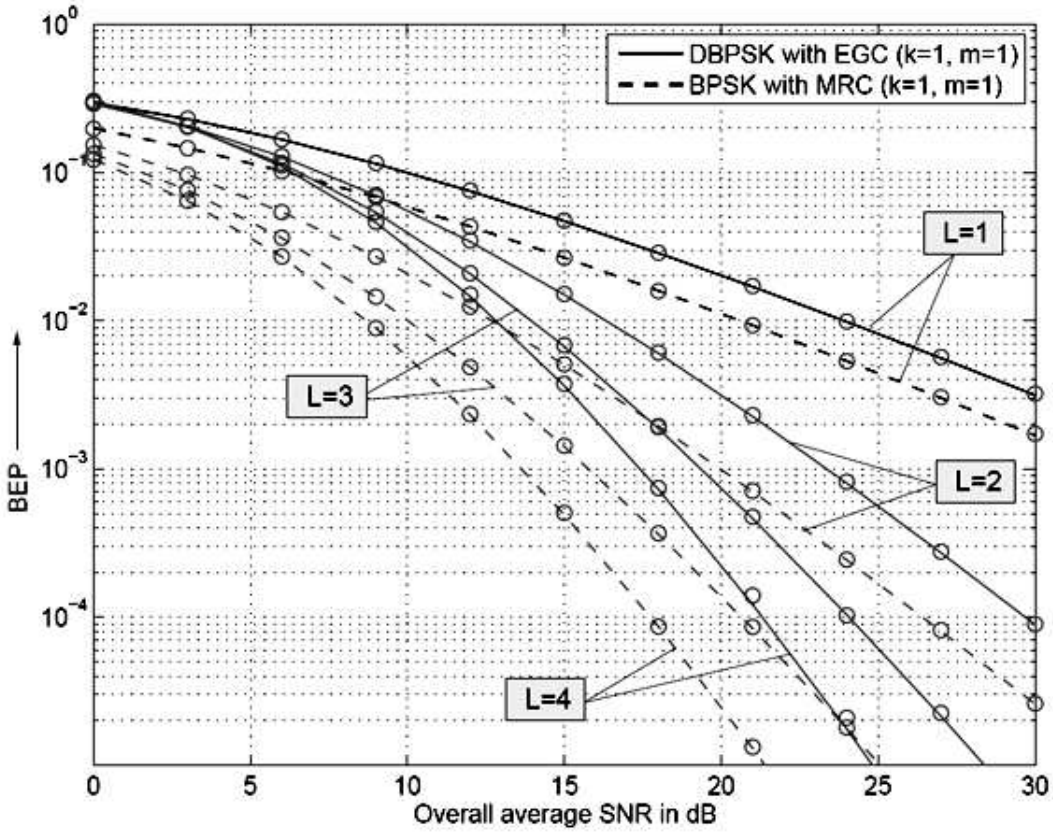

Figure 5.2: Average BEP $\bar{P}_b(\theta)$ versus overall average SNR $L\theta$ in dB for the case of i.i.d. double Rayleigh fading ($k = 1, m = 1$). Solid lines represent analytical results for DBPSK modulation with EGC at the receiver evaluated based on (4.8) /(4.9) using the values $k = 1.01$ and $m = 0.99$. Dashed lines represent corresponding analytical results for coherent BPSK modulation with MRC at the receiver evaluated based on (3.11), (4.26) using numerical integration. Corresponding simulation results for $k = 1$ and $m = 1$ are indicated by markers '$\circ$' (both for DPSK and PSK modulation).

at the receiver for various examples of i.i.d. cascade Rayleigh/Nakagami–m fading ($k = 1, m \in \{1, 3, 5\}, L \in \{1, 3\}$). For the example $m = 3$, we have also included the average BEP of coherent BPSK modulation with MRC at the receiver. Moreover, for the example $m = 3$, $L = 3$ we have included the asymptotic BEP curves as a reference (dotted lines), which were evaluated based on (4.18)/(4.19) and (4.27) for DBPSK and BPSK modulation, respec-

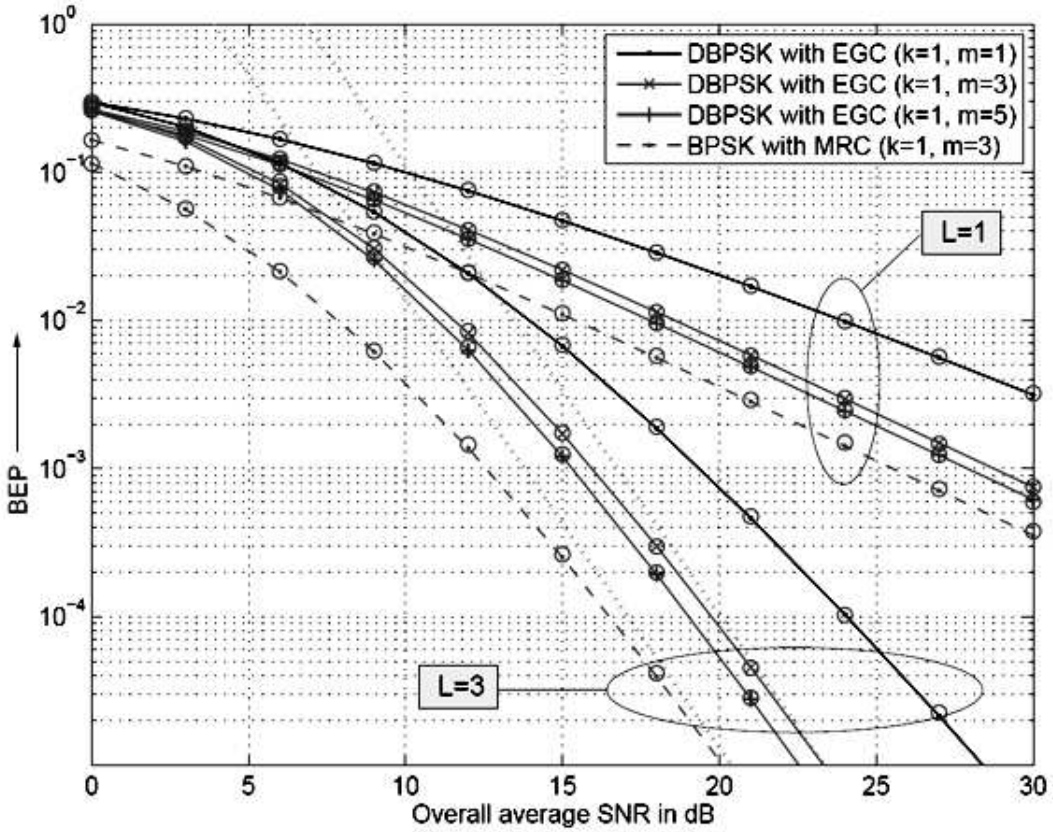

Figure 5.3: Average BEP $\bar{P}_b(\theta)$ versus overall average SNR $L\theta$ in dB for different cases of cascade fading ($k = 1$ and $m \in \{1, 3, 5\}$). Solid lines represent analytical results for DBPSK modulation with EGC at the receiver evaluated based on (4.8) /(4.9) using the values $k = 1.01$ and $m \in \{0.99, 2.99, 4.99\}$, respectively. Dashed lines represent corresponding analytical results for coherent BPSK modulation with MRC at the receiver evaluated based on (3.11), (4.26) using numerical integration. Corresponding simulation results for $k = 1$ and $m \in \{1, 3, 5\}$ are indicated by markers '$\circ$' (both for DPSK and PSK modulation). The dotted lines represent asymptotic BEP curves for the case $m = 3$, $L = 3$ evaluated based on (4.18)/(4.19) for DPSK modulation and based on (4.27) for PSK modulation.

tively. As can be seen, the performance of DBPSK improves significantly, if the fading parameter m is increased from $m = 1$ to $m = 3$. As opposed to this, increasing m further to $m = 5$ yields comparatively small additional perfor-

mance gains, which indicates that the BEP performance is somewhat limited by the small value of the fading parameter k. Another interesting observation is that the performance difference between DBPSK and BPSK modulation at high SNR values is slightly reduced if the fading parameter m is increased. For example, in the case $m = 3$ the performance difference is about 3.3 dB, as opposed to 3.8 dB in the case of double Rayleigh fading, cf. Fig. 5.2. Finally, we again note that the analytical results (evaluated based on (4.8) and (4.9) using the values $k = 1.01$ and $m \in \{0.99, 2.99, 4.99\}$) and the simulation results for $k = 1$ and $m \in \{1, 3, 5\}$ are in good agreement for all considered cases. Moreover, the asymptotic BEP curves accurately represent the behavior of the BEP curves at high SNR values, which corroborates our asymptotic analysis in Section 4.3.1.

5.3.2 Correlated Composite Shadowing and Multipath Fading

Next, we consider the BEP performance of DBPSK modulation over L diversity branches that are subject to correlated composite shadowing and multipath fading (cf. Section 4.2 and 4.3.2). Fig. 5.4 presents numerical results for the average BEP $\bar{P}_b(\theta)$ as a function of the overall average received SNR $L\theta$ in dB for the case $k = 3$ and $m = 1$ (mild shadowing) and $L \in \{1, \ldots, 4\}$. Solid lines represent analytical results evaluated based on (4.15) , using the values $k = 3.01$ and $m = 0.99$. Dashed lines represent analytical results for coherent BPSK modulation with MRC at the receiver (for the cases $L \in \{1, 3, 4\}$), evaluated based on (3.16) and (4.26) using the same values $k = 3.01$ and $m = 0.99$. Corresponding simulation results for $k = 3$ and $m = 1$, obtained by Monte–Carlo simulations over a large number of independent channel realizations, are indicated by markers '$\circ$' (both for DPSK and PSK modulation). As can be seen, the analytical results and the simulation results are in good agreement, which corroborates our analysis in Section 4.2. Note

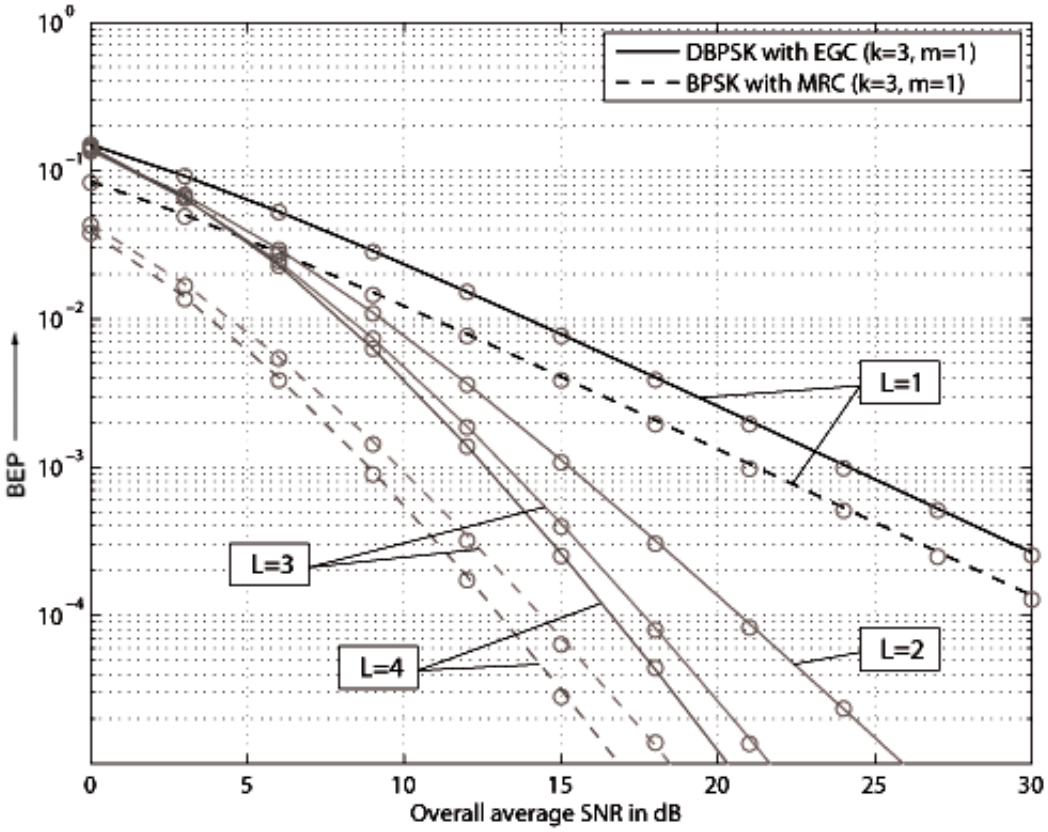

Figure 5.4: Average BEP $\bar{P}_{\mathrm{b}}(\theta)$ versus overall average SNR $L\,\theta$ in dB for the case $k=3$ and $m=1$ (mild shadowing). Solid lines represent analytical results for DBPSK modulation with EGC at the receiver evaluated based on (4.15) using the values $k=3.01$ and $m=0.99$. Dashed lines represent corresponding analytical results for coherent BPSK modulation with MRC at the receiver evaluated based on (3.16) , (4.26) using numerical integration. Corresponding simulation results for $k=3$ and $m=1$ are indicated by markers 'o' (both for DPSK and PSK modulation).

that significant diversity gains are accomplished in the case $L > 1$, both in the case of DPSK and PSK modulation. As can be seen, the general behavior of the BEP curves is the same for coherent and non–coherent transmission (similar to the case of i.i.d. cascade Rayleigh/Nakagami–m fading). The asymptotic advantage of BPSK over DBPSK modulation is about 3 dB, similar to the case of pure Rayleigh fading.

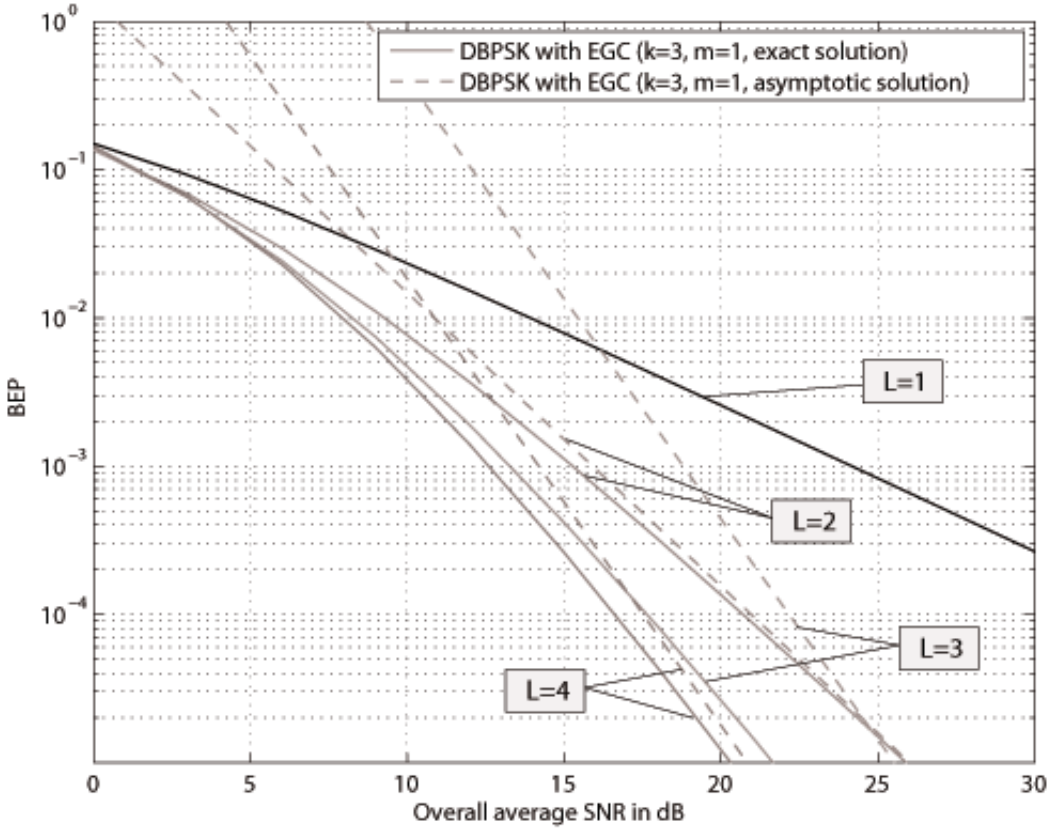

Figure 5.5: Average BEP $\bar{P}_{\rm b}\,(\theta)$ versus overall average SNR $L\,\theta$ in dB for the case $k=3$ and $m=1$ (mild shadowing). Solid lines represent analytical results for DBPSK modulation with EGC at the receiver, evaluated based on (4.15) using the values $k=3.01$ and $m=0.99$. Dashed lines represent corresponding asymptotic results evaluated based on (4.30) .

In Fig. 5.5, we compare the exact analytical BEPs for DPSK modulation according to (4.15) with the asymptotic BEPs according to (4.30) .[4] As earlier, the values $k = 3.01$ and $m = 0.99$ were employed for evaluating the expressions (4.15) and (4.30) . It can be seen that convergence is comparatively fast for the cases $L = 2$ and $L = 4$. In particular, the BEP curves exhibit the predicted diversity orders of $d = 2m = 2$ and $d = k = 3$, respectively. However, as

[4]For BPSK modulation with MRC at the receiver we have obtained very similar results (not depicted) by evaluating asymptotic BEPs according to (4.33) and comparing them with the corresponding analytical BEPs according to (3.16) and (4.26).

discussed in Section 4.3.2, in the case $L = 3$ convergence is very slow, since $k \approx mL$. In this example, SNR values on the order of 100 dB are required, until the exact analytical BEP (4.15) approaches the asymptotic BEP (4.30) and assumes the predicted asymptotic diversity order of $d = 3m \approx k \approx 3$. Note that since the maximum diversity order is accomplished for $L = 3$, the relative performance advantage of $L > 3$ branches is comparatively small in this example.

Finally, in Fig. 5.6 numerical performance results for the case $k = 1$ and $m = 3$ (severe shadowing) and $L \in \{1, 4\}$ are presented. Again it can be seen that the analytical results (solid lines for DBPSK and dashed lines for BPSK modulation) and the simulation results (markers '$\circ$') are in good agreement. The analytical results for DBPSK and BPSK modulation were again evaluated based on (4.15) and (3.16) , (4.26), respectively, using the values $k = 1.01$ and $m = 2.99$. Interestingly, in contrast to the case of mild shadowing, $L > 1$ branches offer no diversity benefit at all. As can be seen, in the case of DBPSK modulation the BEP curve for $L = 4$ is even slightly worse than the BEP curve for $L = 1$ (due to the SNR normalization). The BEP curves for $L = 2$ and $L = 3$ (not depicted) lie in between the curves for $L = 1$ and $L = 4$. As predicted by the asymptotic BEP (4.30) , included here for the case $L = 4$ (dotted line), the BEP curves of DBPSK for $L \geq 1$ branches are all characterized by the same asymptotic diversity order of $d = k = 1$. Also note that the convergence of the asymptotic BEP (4.30) to the exact BEP (4.15) is comparatively fast in this example. Finally, we note that while in the case of BPSK modulation the asymptotic diversity order is the same as for DBPSK modulation, the order of the curves is swapped here, i.e., $L = 4$ offers a slight performance advantage over $L = 1$ (the BEP curves for $L = 2$ and $L = 3$ were again found in between the curves for $L = 1$ and $= 4$).

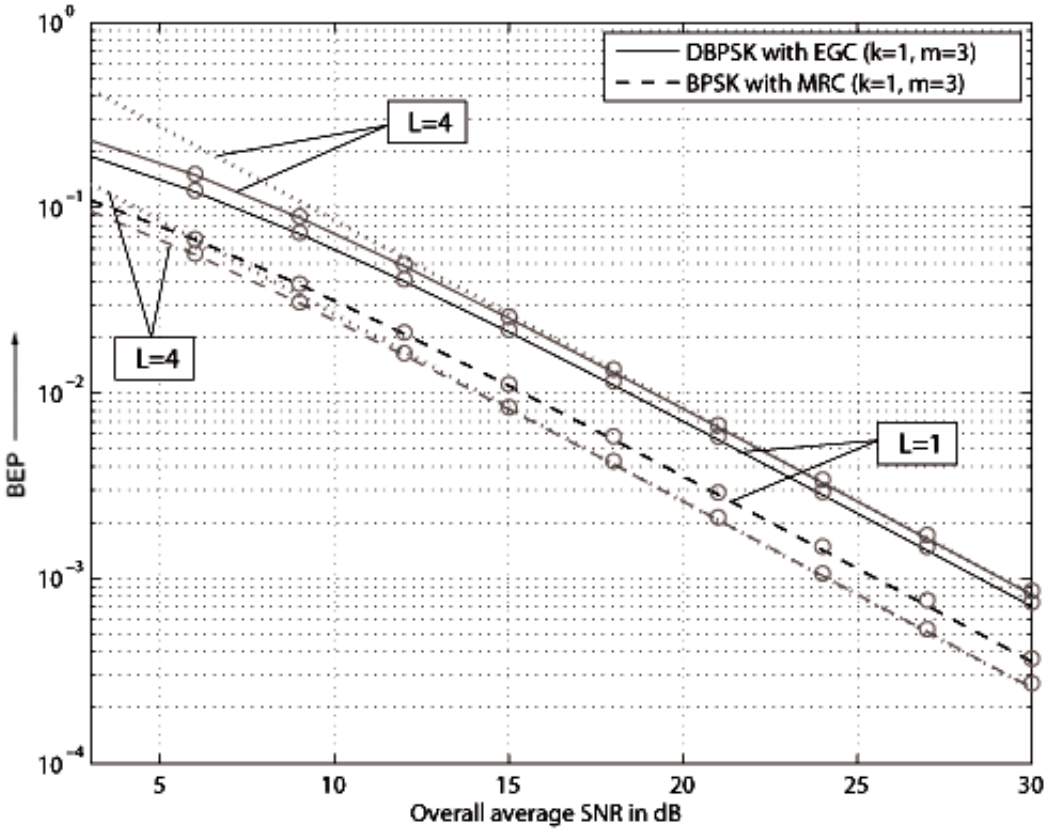

Figure 5.6: Average BEP $\bar{P}_{\mathrm{b}}(\theta)$ versus overall average SNR $L\,\theta$ in dB for the case $k=1$ and $m=3$ (severe shadowing). Solid lines represent analytical results for DBPSK modulation with EGC at the receiver evaluated based on (4.15) using the values $k=1.01$ and $m=2.99$. Dashed lines represent corresponding analytical results for coherent BPSK modulation with MRC at the receiver evaluated based on (3.16) , (4.26) using numerical integration. Corresponding simulation results for $k=1$ and $m=3$ are indicated by markers 'o' (both for DPSK and PSK modulation). The dotted lines represent asymptotic BEP curves for the case $L=4$ evaluated based on (4.30) for DPSK modulation and based on (4.33) for PSK modulation.

5.3.3 Performance of M–ary Modulation Schemes

Finally, we present some numerical performance results for M–ary modulation. As an example, we focus on the case of DQPSK and coherent quaternary

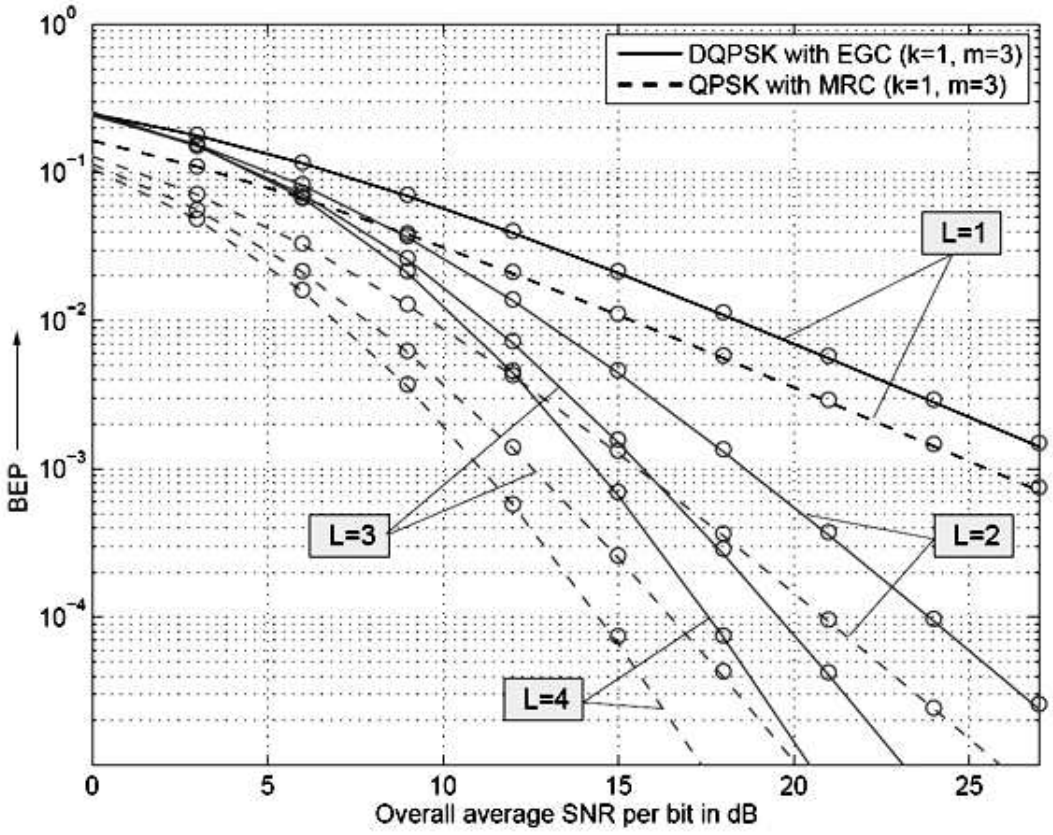

Figure 5.7: Average BEP $\bar{P}_b(\theta)$ versus overall average SNR per bit $L\theta/2$ in dB for the case of cascade fading with $k = 1$ and $m = 3$. Solid lines represent analytical results for DQPSK modulation with EGC at the receiver evaluated based on (3.11) and (5.1) using the values $k = 1.01$ and $m = 2.99$. Dashed lines represent corresponding analytical results for coherent QPSK modulation with MRC at the receiver evaluated based on (3.11) and (4.26) using numerical integration. Corresponding simulation results for $k = 1$ and $m = 3$ are indicated by markers 'o' (both for DPSK and PSK modulation).

PSK (QPSK) modulation over L i.i.d. cascade Rayleigh/ Nakagami–m fading branches with $k = 1$ and $m = 3$. Fig. 5.7 displays the corresponding average BEPs $\bar{P}_b(\theta)$ versus the overall average received SNR per bit $L\theta/2$ in dB for $L \in \{1, \ldots, 4\}$ diversity branches. The analytical results for DQPSK modulation with EGC at the receiver (solid lines) were evaluated based on (3.11) and (5.1) via numerical integration using the values $k = 1.01$ and $m = 2.99$. The

analytical results for coherent QPSK modulation with MRC at the receiver (dashed lines) were evaluated based on (3.11) and (4.26), exploiting the fact that the average BEP of QPSK with Gray mapping is identical to that of BPSK modulation. As can be seen, the basic behavior of the BEP curves is very similar to the case of DBPSK/BPSK modulation.[5] In particular, the asymptotic slope of the BEP curves as well as the performance difference between DQPSK and QPSK modulation is the same as in the case of binary transmission (cf. Fig. 5.3). Again, we note that the analytical results and the simulation results are in good agreement, which corroborates our analysis in Section 5.

[5]We have made the same observation for the case of correlated composite shadowing and multipath fading (not depicted).

Chapter 6

1 Conclusion

In this thesis, we have focused on the receiver design for DSTM over correlated MIMO channels. In addition, the performance analysis of DPSK and non–coherent FSK over generalized fading channels is considered.

For DSTM receiver design, we have derived novel MSDD and low–complexity MS–DFDD receivers for DSTM in spatially correlated fading. We have compared MS–DFDD with previously proposed SP- and VP–DFDD, and shown that SP- and VP–DFDD are equivalent at high SNR. In contrast to VP–DFDD, MS–DFDD performs spatial whitening of the prediction error and thus exploits spatial fading correlations in an optimum manner.

The generalized K–fading model, which is characterized by two fading parameters, $k > 0$ and $m > 0$, is versatile enough to cover both scenarios with cascade multipath fading and scenarios with composite shadowing and multipath fading. In this thesis, we have derived closed–form expressions for the BEP of DBPSK modulation and binary non–coherent FSK modulation over L generalized K–fading links. In particular, we have considered the case of independent fading across links, which is relevant for cascade multipath fading scenarios, and the case of correlated composite shadowing and multipath fading. Moreover, we have conducted an asymptotic performance analysis for high SNR values and have studied the resulting diversity orders for various cases. We have also discussed the extension of our results to M–ary modulation

schemes. Our results have shown that there is an interesting interplay between the two fading parameters k and m. In the case of independent fading, the smaller of the two fading parameters limits the asymptotic diversity order. Similarly, in the case of correlated composite shadowing and multipath fading, the asymptotic diversity order is always limited by either the shadowing effect or the multipath fading, depending on which one of the two fading effects is more severe. Moreover, for both scenarios we have shown that the diversity order of the considered non–coherent transmission schemes is, in fact, the same as in the case of coherent transmission. Finally, numerical performance results were presented, in order to illustrate the above findings, and our analytical performance results were corroborated by means of Monte–Carlo simulations.

Some recommendations for future work may include the study of amplify–and–forward and/or decode–and–forward relaying under general K–fading (on each link). One could again study the interplay of shadowing and multipath fading. Since the individual nodes are spatially distributed on a larger scale, the assumption of independent fading on each link would apply.

Bibliography

[1] B. M. Hochwald and W. Sweldens. Differential unitary space–time modulation. *IEEE Trans. Commun.*, 48:2041–2052, December 2000.

[2] D. Divsalar and M. K. Simon. Multiple symbol differential detection of MPSK. *IEEE Trans. Commun.*, 38(3):300–308, March 1990.

[3] P. Ho and D. Fung. Error performance of multiple–symbol differential detection of PSK signals transmitted over correlated Rayleigh fading channels. *IEEE Trans. Commun.*, 40(10):1566–1569, October 1992.

[4] B. Allen, Y. Kuroda, F. Said, and A. Aghvami. Comparison of coherent and differential space-time block codes over spatially correlated channels. *IEEE Trans. Consumer Electronics*, 50:1232–1236, November 2004.

[5] X. Cai and G. Giannakis. Differential space–time modulation with eigen–beamforming for correlated MIMO fading channels. *IEEE Trans. Signal Processing*, 54:1279–1288, April 2006.

[6] V. Nguyen. A differential space–time modulation scheme for correlated Rayleigh fading channels: Performance analysis and design. *IEEE Trans. Signal Processing*, 55:299–312, January 2007.

[7] P. Tarasak, H. Minn, and V. K. Bhargava. Linear prediction receiver for differential space–time block codes with spatial correlation. *IEEE Commun. Lett.*, 7(11):543–545, November 2003.

[8] D. Tse and P. Viswanath. *Fundamentals of Wireless Communication*. New York: Cambridge University Press, 2005.

[9] V. Erceg, S. Fortune, J. Ling, Jr. A. Rustako, and R. Valenzuela. Comparisons of a computer–based propagation prediction tool with experimental data collected in urban microcellular environments. *IEEE J. Selected Areas Commun.*, 15(4):677–684, May 1997.

[10] J. Salo, H. M. El-Sallabi, and P. Vainikainen. Impact of double–Rayleigh fading on system performance. In *Proc. Int. Symp. on Wireless Pervasive Computing (ISWPC)*, Phuket, Thailand, January 2006.

[11] M. Uysal. Diversity analysis of space–time coding in cascaded Rayleigh fading channels. *IEEE Commun. Letters*, 10(3):165–167, March 2006.

[12] N. H. Tran, H. H. Nguyen, and T. Le-Ngoc. Application of signal space diversity in BICM–ID over cascaded Rayleigh fading channels. In *Proc Int. Conf. Commun. (ICC)*, pages 4011–4016, Glasgow, Scotland, June 2007.

[13] M. K. Simon and M.-S. Alouini. *Digital Communication Over Fading Channels*. John Wiley & Sons, Hoboken, NJ, 2nd edition.

[14] I. M. Kostic. Analytical approach to performance analysis for channel subject to shadowing and fading. *IET Proc. Commun.*, 152(6):821–827, April 2006.

[15] P. S. Bithas, N. C. Sagias, P. T. Mathiopoulos, G. K. Karagiannidis, and A. A. Rontogiannis. On the performance analysis of digital communications over generalized–K fading channels.

[16] R. Schober and L. Lampe. Noncoherent receivers for differential space–time modulation. *IEEE Trans. Commun.*, 50:768–777, May 2002.

[17] G. Reinsel. *Elements of Multivariate Time Series Analysis*. Springer, Berlin, 1993.

[18] V. Pauli and L. Lampe. Tree–search multiple–symbol differential decoding for unitary space–time modulation. *IEEE Trans. Commun.*, 55(8):1567–1576, August 2007.

[19] E. Chiavaccini and G. M. Vitetta. Further results on Tarokh's space–time differential technique. *IEEE Trans. Commun.*, 51(7):1093–1101, July 2003.

[20] W. Kottermann, G. Pedersen, K. Olesen, and P. Eggers. Correlation properties for radio channels from multiple base stations to two antennas on a small handheld terminal. In *Proc. IEEE Veh. Techn. Conf. (VTC)*, pages 462–466, September 2002.

[21] R. Schober and W. Gerstacker. Decision–feedback differential detection based on linear prediction for MDPSK signals transmitted over Ricean fading channels. *IEEE J. Select. Areas Commun.*, 18(3):391–402, March 2000.

[22] P. Shankar. Error rates in generalized shadowed fading channels. *Wireless Personal Commun.*, 28(4):233–238, February 2004.

[23] I. S. Gradsheteyn and I. M. Ryzhik. *Table of Integrals, Series, and Products*. Academic Press, New York, NY, 7th edition, 1994.

[24] M. Abramowitz and I. A. Stegun (Eds.). *Handbook of Mathematical Functions*. National Bureau of Standards, Washington, D.C, 10th edition, 1972.

[25] J. G. Proakis. *Digital Communications*. McGraw-Hill, New York, 4th edition, 2001.

[26] M.-S. Alouini and A. J. Goldsmith. A unified approach for calculating error rates of linearly modulated signals over generalized fading channels. *IEEE Trans. Commun.*, 47(9):1324–1334, September 1999.

[27] G. Arfken. *Mathematical Methods for Physicists*. Academic Press, Orlando, FL, 3rd edition, 1985.